

# ARSAR-Net: Adaptively Regularized SAR Imaging Network via Non-matrix-inversion ADMM

Shiping Fu, Yufan Chen, Zhe Zhang, Xiaolan Qiu, Qixiang Ye

**Abstract**—Deep unfolding networks have constituted an emerging method for synthetic aperture radar (SAR) imaging. However, baseline unfolding networks, when unfolded from the alternating direction method of multipliers (ADMM), lack generalization capability across scenes as the regularizers are empirically designed. In this study, we introduce a learnable regularizer to the unfolding network and create an adaptively regularized SAR imaging network (ARSAR-Net), which pursues generalization capability across scenes, including varying sparsity levels and heterogeneous scenes with offshore ships, islands, urban areas, and mountainous terrain. In practice, the vanilla ARSAR-Net suffers from inherent structural limitations in 2D signal processing, primarily due to its reliance on matrix inversion. To conquer this challenge, we introduce the non-matrix-inversion ADMM algorithm, which replaces inefficient matrix inversion with efficient linear approximations. Extensive validation through simulated and real-data experiments (including GF-3 satellite echoes) demonstrates ARSAR-Net’s triple advantage: (1) 50% faster imaging speed compared to existing unfolding networks, (2) up to 2.0 dB PSNR improvement in imaging quality, and (3) enhanced adaptability to complex heterogeneous scenes. These advancements establish a new paradigm for computationally efficient and generalizable SAR imaging systems.

**Index Terms**—Synthetic aperture radar imaging, Sparse microwave imaging, Adaptive regularization, Non-matrix-inversion ADMM, Deep unfolding network.

## I. INTRODUCTION

Synthetic aperture radar (SAR), as an important microwave imaging technique, has been widely utilized in diverse applications including remote sensing, earth observation, mapping, forestry, agriculture and military reconnaissance [1]–[4], due to its unique all-weather/all-time operational reliability and high-resolution imaging capacity [5]. Conventional widely-used SAR imaging techniques, such as the range-Doppler algorithm (RDA) [6] and the chirp scaling algorithm (CSA) [7], typically use matched filtering (MF) techniques. In recent decades, sparse signal processing, represented by compressed sensing (CS) theory, has been introduced into SAR imaging. Sparse SAR imaging not only enables successful imaging from fewer measurements than those traditionally required by the Nyquist theory, but also improves SAR imaging performance, such as achieving lower sidelobes and better ambiguity suppression [8]. Although sparse SAR imaging has been widely adopted for sparse scenes, the generalization capability of these methods remains insufficient, as the hand-crafted regularizers, often based on the  $\ell_1$ -norm, lack adaptability

when processing echo signals from scenes of various sparsity degrees or different scene types.

Most recently, unfolding networks [9], Fig. 1, have emerged as a promising method for SAR imaging. These networks are constructed by unfolding the iterative reconstruction algorithms such as the iterative shrinkage-thresholding algorithm (ISTA) [10] and the alternating direction method of multiplier (ADMM) [11] into a neural network with learnable parameters. Addressing the computational complexity issue, approximated observation operators that are constructed from MF algorithms [12] are also adopted. In this way, these approaches take advantage of both model-driven algorithms and data-driven networks, achieving enhanced performance while enjoying interpretability. However, the baseline unfolding networks remain challenged by scene generalization capability as the regularizers are simple and empirically chosen. Furthermore, these networks are constrained by the structural limitations of the 2D signal processing, which typically relies on the matrix inversion operation. Efficient alternatives to the inefficient matrix inversion in the ADMM-based unfolding networks need to be explored.

### A. Related work

Compressed sensing-inspired regularization approaches [13] have shown great potential when reconstructing sparse signals from limited observation data. As a classical regularizer,  $\ell_1$ -norm minimization [14] is commonly formulated as a regularized inverse optimization problem, reconstructing target scenes by solving an objective function [15]. Considering the scattered field of SAR is sparse, iterative algorithms such as orthogonal matching pursuit (OMP) [16], compressive sampling matching pursuit (CoSaMP) [17], iterative shrinkage-thresholding algorithm (ISTA), and fast iterative shrinkage-thresholding algorithm (FISTA) [18] can be applied. While effective in sparse scenes, these methods struggle to define a general sparse basis for scenes of different sparsity degrees.

To address the adaptive sparsity issue, structural sparse representation [19], [20] is proposed to formulate SAR image reconstruction and sparse space updating as a joint optimization problem. Combined dictionaries [21] with structured sparsity were also proposed for adaptive sensing. These improved approaches with structural sparse transforms can directly process downsampling raw data. However, they remain challenged by space-borne SAR imaging when handling large-scale measurement matrices.

To conquer the challenge of large-scale matrices, approximated observation operators based on matched filters are proposed to reconstruct sparse scenes from downsampling

Manuscript for Review. Shiping Fu, Yufan Chen and Qixiang Ye are with the University of Chinese Academy of Sciences, Beijing, China. Xiaolan Qiu and Zhe Zhang are with the Aerospace Information Research Institute of Chinese Academy of Sciences, Beijing, China.

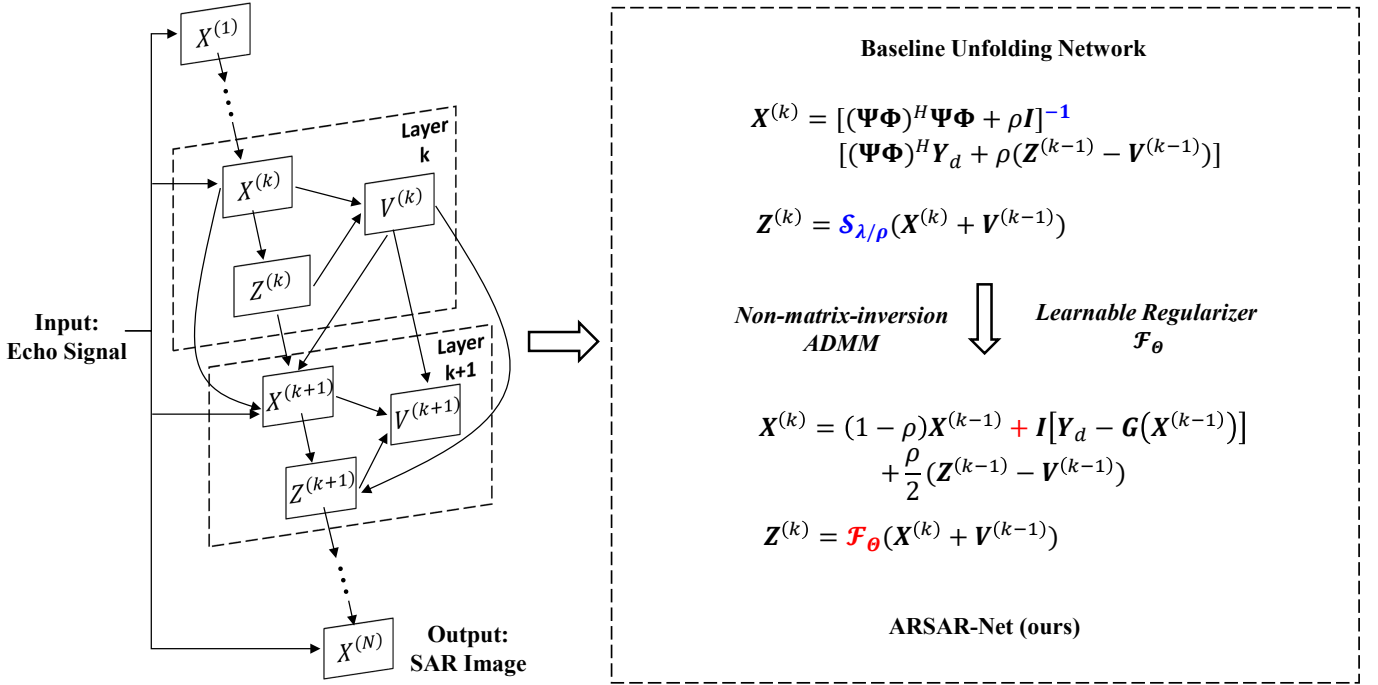


Fig. 1. SAR imaging with unfolding networks. We upgrade the baseline unfolding network to ARSAR-Net by introducing a non-matrix-inversion ADMM and a learnable regularizer.

data for high-quality imaging with efficiency. Jiang et al. [22] constructed a decoupling operator through the chirp scaling algorithm, and proposed an efficient  $\ell_q$  regularization algorithm, which reduces the computational complexity from the square order to the linear order. While these methods address data storage and processing problems, they face two major challenges. First, compressed sensing methods typically involve numerous hyperparameters that need to be manually tuned. Secondly, conventional sparse representation methods require both a specific sparse basis and a predefined regularization tailored to the target SAR scattering field. Consequently, their adaptability is constrained by the need for manual hyperparameter tuning and the reliance on specific prior modeling.

As a data-driven approach, deep learning (DL) methods can learn representations from the training data, avoiding hand-crafted modeling and parameter tuning. In the signal and image processing field, deep neural networks (DNNs) demonstrate remarkable effectiveness, offering innovative solutions for SAR imaging [23]–[25]. Gao et al. [26] explored the potential of applying DNNs to radar imaging using a complex-valued convolutional neural network (CNN). For moving target imaging, Lu et al. [27] proposed an enhanced U-Net architecture with a refocusing method based on the range-doppler algorithm. Mu et al. [28] applied CNN to multiple target imaging, improving imaging quality and efficiency with significant margins.

In contrast to CNNs, unfolding networks take advantage of the interpretability of iterative algorithms and the generalization capacity of DL [29]. DUNs transform each iteration of conventional compressed sensing-driven iterative algorithms into a corresponding layer of a deep network,

resulting in unfolding networks. Specifically, each iteration of iterative algorithms is transformed into a trainable neural network layer, forming the unfolding networks. Such networks achieved enhanced imaging performance and interpretability and have been widely investigated. For instance, a representative unfolding network, AF-AMPNet [30], employs an unfolding architecture for inverse synthetic aperture radar (ISAR) imaging. LFIST-Net [31] constructs a lightweight holographic network based on FISTA, achieving higher flexibility for 3D millimeter-wave imaging.

Motivated by these studies, deep unfolding methods for SAR imaging have emerged [32], [33]. Mason et al. [34] integrated SAR imaging with an ISTA-based autoencoder network, achieving superior convergence rates and reduced reconstruction errors. Li et al. [35] proposed a target-oriented SAR imaging model which incorporates generalized regularization to enhance the signal-to-clutter ratio (SCR) of reconstructed images. For non-sparse scenes, An et al. [36] formulated SAR imaging as a joint low-rank and sparse matrix recovery problem with ADMM, creating the LRSR-ADMM-Net. Kang et al. [37] proposed RDA-Net, an unfolding imaging network that reconstructs non-sparse SAR scenes through learned compensation matrices derived from the RDA. However, this implementation of learnable compensation matrices requires substantial storage resources, posing computational challenges in high-resolution imaging. Zhang et al. [38] proposed the ISTA-based unfolding network and addressed the storage issue by utilizing CSA-generated imaging operators. Despite the progress on the storage issue, the computational efficiency remains a challenge.

ADMM, an iterative optimization algorithm for image re-

construction, has been adopted to design unfolding networks. One of the primary characteristics of ADMM is its modular structure, which facilitates embedding reconstruction methods, such as  $\ell_1$ -norm [39], TV-norm [40], and denoisers. However, conventional regularization methods are often constrained by their predefined mathematical formulations, which restrict their optimization capabilities in complex scenes. To solve, researchers plugged denoisers into ADMM. Venkatakrisnan et al. [41] replaced the regularizer with a denoiser for magnetic resonance imaging (MRI) reconstruction. Teodoro et al. [42] incorporated a Gaussian mixture model into ADMM for optical image denoising. For SAR imaging, Fan et al. [43] developed a multi-agent consensus equilibrium mechanism by embedding composite regularization into ADMM, achieving good results in azimuth ambiguity suppression, multi-feature enhancement, and speckle reduction. Wang et al. [44] integrated denoisers into a linearized ADMM, which delivered high performance and efficiency in 3D SAR imaging. Despite the progress, ADMM-based methods for 2D SAR imaging are limited by the intrinsic coupling between range and azimuth dimensions, which requires the vectorization of 2D radar signals into 1D vectors [45]. The dimensional coupling prevents the direct application of matrix inversion in the ADMM frameworks, making it challenging to find the explicit derivation of iterative solutions.

In recent years, learnable regularization, which pursues regularization adaptability in a data-driven fashion, has emerged as a groundbreaking approach. This adaptability makes it suitable for image reconstruction within the ADMM framework. Based on this point, Yang et al. [46] developed an optimization module using CNNs and nonlinear piecewise functions, embedding it as a subproblem of the ADMM. Their proposed ADMM-CSNet demonstrated superior performance and computational efficiency in both MRI and optical image reconstruction. The advances of these methods inspire the ARSAR-Net in this study.

## B. Contributions

In this paper, we propose an adaptively regularized SAR imaging network (ARSAR-Net) to enhance generalization capability across scenes with varying sparsity degrees.<sup>1</sup> ARSAR-Net is built upon an unfolding network that follows the framework of ADMM without matrix inversion. To overcome the limitations of empirically designed regularizers, ARSAR-Net introduces a learnable regularizer, enabling the model to adapt to diverse scene characteristics. In Fig. 1, we show the framework of ARSAR-Net and its improvements upon the baseline unfolding network. The contributions of this study are summarized as follows.

- We introduce the non-matrix-inversion ADMM and develop an enhanced 2D SAR imaging model. The proposed model reformulates the imaging procedure and replaces the inefficient matrix inversion with an efficient linear approximation derived from Taylor expansion.
- Based on the proposed non-matrix-inversion ADMM, we design ARSAR-Net, which incorporates a learnable

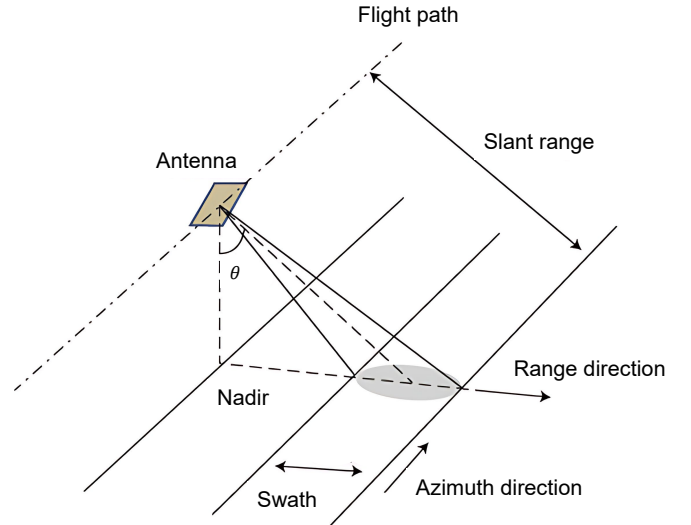


Fig. 2. Geometric Structure of SAR Imaging System(Credit: NASA). [47]

regularizer to improve the generalization capability of imaging models across scenes.

- Experimental results demonstrate the superiority of ARSAR-Net over existing methods. When handling real echo signals, the proposed method demonstrates a 50% acceleration in imaging speed compared to recent unfolding networks, while simultaneously improving imaging PSNR by up to 2 dB.

The remainder of this paper is organized as follows. Section II discusses the 2D SAR imaging model based on non-matrix-inversion ADMM. Section III provides a detailed description of the adaptive regularized SAR imaging network. Section IV presents experimental results and performance analysis. Finally, Section V concludes the paper.

## II. NON-MATRIX-INVERSION ADMM ALGORITHM

To make the section self-contained, we first introduce the 1D and 2D SAR imaging algorithms within the conventional ADMM framework. However, the integration of 2D SAR imaging algorithms with ADMM encounters structural limitations, rendering conventional ADMM ineffective for 2D SAR imaging. To address this issue, we introduce the non-matrix-inversion ADMM framework and develop an enhanced 2D SAR imaging model based on it.

### A. 1D Imaging Model via Observation Matrix and ADMM

In this study, the vertical side-looking strip mode is employed to obtain SAR echo signals as shown in Fig. 2. The 1D imaging model establishes a mathematical relationship between the radar echo signal and the scattering coefficients of the observed scene through an observation matrix  $\Phi \in \mathbb{C}^{MN \times MN}$ . For numerical processing, the observation area is discretized to a grid of  $M \times N$  scattering centers, where the indices  $m = 1, 2, \dots, M$  and  $n = 1, 2, \dots, N$  denote discrete positions along the range and azimuth directions, respectively. This discretization allows the scattering coefficients to be

<sup>1</sup>Code is available at <https://github.com/ShipenFyu/ARSAR-Net>.

denoted as a 2D matrix  $\mathbf{X} \in \mathbb{C}^{M \times N}$ , which is vectorized to  $\mathbf{x} = \text{vec}(\mathbf{X}) \in \mathbb{C}^{MN \times 1}$ . Similarly, the echo signal  $\mathbf{Y} \in \mathbb{C}^{M \times N}$  is vectorized into  $\mathbf{y} = \text{vec}(\mathbf{Y}) \in \mathbb{C}^{MN \times 1}$ . Through the downsampling matrix  $\Psi \in \mathbb{R}^{M'N' \times MN}$ , the downsampled echo signal  $\mathbf{Y}_d \in \mathbb{C}^{M' \times N'}$  is vectorized into  $\mathbf{y}_d = \text{vec}(\mathbf{Y}_d) \in \mathbb{C}^{M'N' \times 1}$ .

When the observation scene exhibits sufficient sparsity and the measurement matrix  $\Phi$  satisfies the restricted isometry property (RIP) [48], the scattering coefficients  $\mathbf{x}$  can be reconstructed through solving the  $\ell_1$ -norm optimization problem, through an ADMM algorithm.

ADMM decomposes the primal problem into variable-separable subproblems through the introduction of dual variables, thereby enabling more flexible handling of each subproblem. This flexibility allows specialized optimization strategies to be employed for different types of regularization, making ADMM particularly well-suited to a wide range of regularization terms. Furthermore, ADMM reinforces constraints via a quadratic penalty term within the augmented Lagrangian framework [49], which guarantees a better convergence property than other iterative methods.

Through ADMM, the primal optimization problem is decomposed into two separable parts involving the variables  $\mathbf{x}$  and  $\mathbf{z}$ , as

$$\begin{aligned} \min_{\mathbf{x}} \|\mathbf{y}_d - \Psi\Phi\mathbf{x}\|_2^2 + \lambda\|\mathbf{z}\|_1 \\ \text{s.t. } \mathbf{z} = \mathbf{x}. \end{aligned} \quad (1)$$

Through constructing the augmented Lagrangian function with a quadratic penalty term incorporated, where the variable  $\mathbf{u}$  is the dual variable and  $\rho$  the penalty parameter, we have

$$\begin{aligned} L_\rho(\mathbf{x}, \mathbf{z}, \mathbf{u}) = \|\mathbf{y}_d - \Psi\Phi\mathbf{x}\|_2^2 + \lambda\|\mathbf{z}\|_1 \\ + \frac{\rho}{2}\|\mathbf{z} - \mathbf{x}\|_2^2 + \langle \mathbf{u}, \mathbf{z} - \mathbf{x} \rangle. \end{aligned} \quad (2)$$

The  $k$ -th iteration of ADMM is expressed in scaled form by grouping the linear and quadratic terms of the above Lagrangian function in Eq. 2 and introducing a scaled dual variable  $\mathbf{v} = \frac{1}{\rho}\mathbf{u}$ , as

$$\begin{cases} \mathbf{x}^{(k)} = \arg \min_{\mathbf{x}} \|\mathbf{y}_d - \Psi\Phi\mathbf{x}\|_2^2 \\ \quad + \frac{\rho}{2}\|\mathbf{x} - \mathbf{z}^{(k-1)} + \mathbf{v}^{(k-1)}\|_2^2 \\ \mathbf{z}^{(k)} = \arg \min_{\mathbf{z}} \lambda\|\mathbf{z}\|_1 + \frac{\rho}{2}\|\mathbf{x}^{(k)} - \mathbf{z} + \mathbf{v}^{(k-1)}\|_2^2 \\ \mathbf{v}^{(k)} = \mathbf{v}^{(k-1)} + \mathbf{x}^{(k)} - \mathbf{z}^{(k)}. \end{cases} \quad (3)$$

With matrix inversion, Eq. 3 has an explicit solution, formulated as Eq. 4, where  $(\cdot)^H$  denotes the conjugate transposition,  $(\cdot)^{-1}$  the matrix inversion, and

$$\mathcal{S}_{\lambda/\rho}(\boldsymbol{\sigma}) = \text{sign}(\boldsymbol{\sigma}) \max\{|\boldsymbol{\sigma} - \lambda/\rho, 0\}$$

in Eq. 4 is the soft-thresholding function.  $\lambda$  and  $\rho$  are the regularization factor and the penalty parameter, respectively.

As can be seen, the 1D imaging model transforms 2D echo signals and scattering coefficients to 1D vectors, causing a quadratic increase in the observation matrix size. For example, converting an  $N \times N$  echo matrix into a vector results in a  $N^2 \times N^2$  observation matrix  $\Phi$ . This increases both storage requirements and computational costs substantially.

### B. 2D Imaging Model via Imaging Operator and ADMM

The imaging model, defined in Sec. II-A, faces significant challenges. The large-scale observation matrix  $\Phi$  imposes substantial computational and storage overhead, while the inherent coupling between azimuth and range dimensions complicates direct matrix decoupling. The matched filter technique avoids these challenges by approximating  $\Phi$  with a series of 1D operators in the azimuth and range directions [12].

Let  $M$  denote the MF imaging procedure. The scattering coefficient matrix  $\mathbf{X}$  is approximately reconstructed by  $\hat{\mathbf{X}} = M(\mathbf{Y})$ . Meanwhile, let  $\tilde{\Phi}$  denote the observation process, where the echo matrix  $\mathbf{Y}$  is obtained as  $\mathbf{Y} = \tilde{\Phi}(\mathbf{X})$ . Let  $H$  denote the inverse MF imaging procedure, as

$$\mathbf{H} = M^{-1} \approx \tilde{\Phi}.$$

Both  $M$  and its approximate inverse  $H$  are efficiently implemented through the chirp scaling algorithm (CSA), which consists of three key phase multiplication stages [50], as (i) Differential range cell migration correction (RCMC); (ii) Range compression and bulk RCMC; and (iii) Azimuth compression. These operations directly construct the imaging operator  $M(\cdot)$  and the approximated observation operator  $H(\cdot)$ , as

$$\begin{aligned} M(\mathbf{Y}) &= \langle \mathbf{F}_r^H \{ \mathbf{F}_r [(Y\mathbf{F}_a) \circ \Theta_s] \circ \Theta_r \} \circ \Theta_a \rangle \mathbf{F}_a^H, \\ H(\mathbf{X}) &= \langle \mathbf{F}_r^H \{ \mathbf{F}_r [(X\mathbf{F}_a) \circ \Theta_a^*] \circ \Theta_r^* \} \circ \Theta_s^* \rangle \mathbf{F}_a^H, \end{aligned} \quad (5)$$

where  $\circ$  denotes the Hadamard product.  $\mathbf{F}_r$  and  $\mathbf{F}_a$  are the FFT matrices along the range and azimuth directions, respectively.  $\mathbf{F}_r^H$  and  $\mathbf{F}_a^H$  denote the IFFT matrices.  $\Theta_s$ ,  $\Theta_r$ , and  $\Theta_a$  are the quadratic phase function for chirp scaling operation, the phase function for range compression and bulk RCMC, and the phase function for azimuth compression and residual phase compensation, respectively.

For better regularization, the  $\ell_1$ -norm is replaced by a function  $\phi(\cdot)$  allowing for arbitrary forms. Upon Eq. 1, the generalized optimization problem is defined upon variables  $\mathbf{X}$  and  $\mathbf{Z}$ , as

$$\begin{aligned} \min_{\mathbf{X}} \|\mathbf{G}(\mathbf{X}) - \mathbf{Y}_d\|_2^2 + \lambda\phi(\mathbf{Z}) \\ \text{s.t. } \mathbf{Z} = \mathbf{X}, \end{aligned} \quad (6)$$

where  $\mathbf{Y}_d \in \mathbb{C}^{M' \times N'}$  and  $\mathbf{X} \in \mathbb{C}^{M \times N}$  are the 2D matrices defined in Sec. II-A, and  $\mathbf{G}(\cdot) = \Psi_r H(\cdot) \Psi_a$  denotes the

$$\begin{cases} \mathbf{x}^{(k)} = [(\Psi\Phi)^H \Psi\Phi + \rho\mathbf{I}]^{-1} [(\Psi\Phi)^H \mathbf{y}_d + \rho(\mathbf{z}^{(k-1)} - \mathbf{v}^{(k-1)})] \\ \mathbf{z}^{(k)} = \mathcal{S}_{\lambda/\rho}(\mathbf{x}^{(k)} + \mathbf{v}^{(k-1)}) \\ \mathbf{v}^{(k)} = \mathbf{v}^{(k-1)} + \mathbf{x}^{(k)} - \mathbf{z}^{(k)} \end{cases} \quad (4)$$

observation operator incorporating the downsampling matrices  $\Psi_r$  and  $\Psi_a$  of the range and azimuth directions, respectively.

Accordingly, an augmented Lagrangian function is constructed, where the variable  $\mathbf{U}$  is the dual variable and  $\rho$  is the penalty parameter, as

$$L_\rho(\mathbf{X}, \mathbf{Z}, \mathbf{U}) = \|\mathbf{Y}_d - \mathbf{G}(\mathbf{X})\|_2^2 + \lambda\phi(\mathbf{Z}) + \frac{\rho}{2}\|\mathbf{Z} - \mathbf{X}\|_2^2 + \langle \mathbf{U}, \mathbf{Z} - \mathbf{X} \rangle. \quad (7)$$

For Eq. 7, the  $k$ -th iteration of ADMM is derived by decomposing into three sequential updates, as

$$\begin{cases} \mathbf{X}^{(k)} = \arg \min_{\mathbf{X}} \|\mathbf{Y}_d - \mathbf{G}(\mathbf{X})\|_2^2 + \frac{\rho}{2}\|\mathbf{X} - \mathbf{Z}^{(k-1)} + \mathbf{V}^{(k-1)}\|_2^2 & (8a) \\ \mathbf{Z}^{(k)} = \arg \min_{\mathbf{Z}} \lambda\phi(\mathbf{Z}) + \frac{\rho}{2}\|\mathbf{X}^{(k)} - \mathbf{Z} + \mathbf{V}^{(k-1)}\|_2^2 & (8b) \\ \mathbf{V}^{(k)} = \mathbf{V}^{(k-1)} + \mathbf{X}^{(k)} - \mathbf{Z}^{(k)} & (8c) \end{cases}$$

where  $\mathbf{V} = \frac{1}{\rho}\mathbf{U}$  is the scaled dual variable.

Different from the imaging model in Sec. II-A, the observation operator  $\mathbf{G}(\cdot)$  is not a single matrix but combines matrix multiplications and Hadamard products, which is formulated as Eq. 9. Limited by the intricate mathematical composition of this operator, the 2D imaging model cannot derive explicit iterative solutions of scattering coefficient  $\mathbf{X}$  via matrix inversion as demonstrated in Eq. 4. Consequently, the conventional ADMM is ill-suited for 2D SAR imaging.

### C. 2D Imaging Model via Non-matrix-inversion ADMM

To resolve the incompatibility between conventional ADMM and 2D SAR imaging, we adopt the non-matrix-inversion ADMM [44], where matrix inversion is replaced by a Taylor expansion-based linear approximation. Based on this, we develop an enhanced 2D SAR imaging model. The solution methods for Subproblem  $\mathbf{X}$  in Eq. 8a and Subproblem  $\mathbf{Z}$  in Eq. 8b are derived as follows.

1) *Subproblem X*: Let  $\mathcal{S}(\mathbf{X}^{(k)})$  denote the objective function to be optimized in the subproblem  $\mathbf{X}$  in Eq. 8a, which is formulated as

$$\mathcal{S}(\mathbf{X}^{(k)}) = \left\| \mathbf{G}(\mathbf{X}^{(k)}) - \mathbf{Y}_d \right\|_2^2 + \frac{\rho}{2} \left\| \mathbf{X}^{(k)} - \mathbf{Z}^{(k-1)} + \mathbf{V}^{(k-1)} \right\|_2^2. \quad (11)$$

We carry out a second-order Taylor expansion of the objective function  $\mathcal{S}(\mathbf{X}^{(k)})$  while truncating higher-order terms. The observation operator  $\mathbf{G}(\cdot)$  integrates three components: linear downsampling matrices, Fourier transform matrices, and

range cell migration correction (RCMC) operators predetermined by radar system parameters. Since all components of  $\mathbf{G}(\cdot)$  exhibit asymptotic linearity under practical radar parameter configurations, the second-order gradient matrix (Hessian matrix) can be approximated as a constant matrix [51], as

$$\begin{aligned} \mathbf{X}^{(k)} &= \arg \min_{\mathbf{X}} \mathcal{S}(\mathbf{X}) \\ &\approx \arg \min_{\mathbf{X}} \mathcal{S}(\mathbf{X}^{(k-1)}) + \nabla \mathcal{S}(\mathbf{X}^{(k-1)})^H (\mathbf{X} - \mathbf{X}^{(k-1)}) \\ &\quad + \frac{1}{2} (\mathbf{X} - \mathbf{X}^{(k-1)})^H \nabla^2 \mathcal{S}(\mathbf{X}^{(k-1)}) (\mathbf{X} - \mathbf{X}^{(k-1)}) \\ &\approx \arg \min_{\mathbf{X}} \mathcal{S}(\mathbf{X}^{(k-1)}) + \nabla \mathcal{S}(\mathbf{X}^{(k-1)})^H (\mathbf{X} - \mathbf{X}^{(k-1)}) \\ &\quad + \frac{L}{2} \left\| \mathbf{X} - \mathbf{X}^{(k-1)} \right\|_2^2, \end{aligned} \quad (12)$$

where  $L$  serves as a constant approximation to the second-order gradient matrix, thereby simplifying the iteration.

Through derivation of the optimization problem Eq. 12, we have the closed-form solution<sup>2</sup>, as

$$\begin{aligned} \mathbf{X}^{(k)} &= \left(1 - \frac{\rho}{L}\right) \mathbf{X}^{(k-1)} + \frac{2}{L} \mathbf{I} \left[ \mathbf{Y}_d - \mathbf{G}(\mathbf{X}^{(k-1)}) \right] \\ &\quad + \frac{\rho}{L} (\mathbf{Z}^{(k-1)} - \mathbf{V}^{(k-1)}), \end{aligned}$$

where  $\mathbf{I}(\cdot)$  denotes the imaging operator with downsampling matrices, which can be formulated as Eq. 10.

When setting  $L = 2$ , we have the explicit solution to the subproblem  $\mathbf{X}$ , as

$$\begin{aligned} \mathbf{X}^{(k)} &= \left(1 - \frac{\rho}{2}\right) \mathbf{X}^{(k-1)} + \mathbf{I} [\mathbf{Y}_d - \mathbf{G}(\mathbf{X}^{(k)})] \\ &\quad + \frac{\rho}{2} (\mathbf{Z}^{(k-1)} - \mathbf{V}^{(k-1)}). \end{aligned} \quad (13)$$

2) *Subproblem Z*: Replacing the empirical regularizer (*e.g.*,  $\ell_1$ -norm) with a function  $\phi(\cdot)$ , the nonlinear proximal operator  $\mathcal{F}(\cdot)$  determined by  $\phi(\cdot)$  is implemented through either model-based denoiser or data-driven neural networks. Consequently, the closed-form solution of subproblem  $\mathbf{Z}$  is formulated as

$$\mathbf{Z}^{(k)} = \mathcal{F}_\Theta(\mathbf{X}^{(k)} + \mathbf{V}^{(k-1)}), \quad (14)$$

where  $\mathcal{F}_\Theta(\cdot)$  is the nonlinear proximal operator, and  $\Theta$  denotes the parameters of the denoiser or neural network.

The computational flowchart of Subproblem  $\mathbf{Z}$  is illustrated in Fig. 3.

3) *Non-Matrix-Inversion ADMM*: By integrating the solutions of these subproblems, we have the non-matrix-inversion ADMM, which avoids matrix inversion to enable efficient 2D SAR imaging, as

<sup>2</sup>Please refer to Appendix A for the detailed derivation.

$$\mathbf{G}(\mathbf{X}) = \Psi_r \langle \mathbf{F}_r^H \{ \mathbf{F}_r [ (\mathbf{X} \mathbf{F}_a) \circ \Theta_a^* ] \circ \Theta_r^* \} \circ \Theta_s^* \rangle \mathbf{F}_a^H \Psi_a \quad (9)$$

$$\mathbf{I}(\mathbf{Y}) = \langle \mathbf{F}_r^H \{ \mathbf{F}_r [ (\Psi_r^H \mathbf{Y} \Psi_a^H \mathbf{F}_a) \circ \Theta_s ] \circ \Theta_r \} \circ \Theta_a \rangle \mathbf{F}_a^H \quad (10)$$

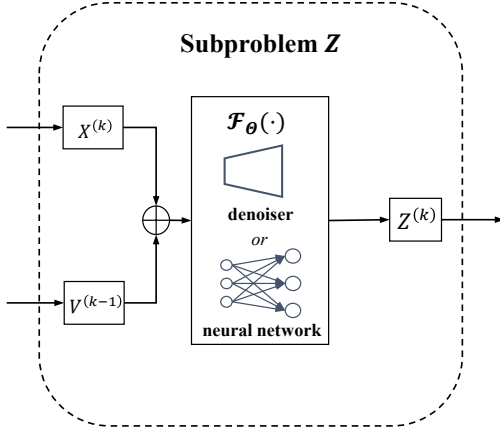


Fig. 3. Computational diagram of subproblem  $Z$

$$\begin{cases} \mathbf{X} : \mathbf{X}^{(k)} = (1 - \frac{\rho}{2})\mathbf{X}^{(k-1)} + \mathbf{I} [\mathbf{Y}_d - \mathbf{G}(\mathbf{X}^{(k-1)})] \\ \quad + \frac{\rho}{2}(\mathbf{Z}^{(k-1)} - \mathbf{V}^{(k-1)}) & (15a) \\ \mathbf{Z} : \mathbf{Z}^{(k)} = \mathcal{F}_\Theta(\mathbf{X}^{(k)} + \mathbf{V}^{(k-1)}) & (15b) \\ \mathbf{V} : \mathbf{V}^{(k)} = \mathbf{V}^{(k-1)} + \mathbf{X}^{(k)} - \mathbf{Z}^{(k)} & (15c) \end{cases}$$

The proposed non-matrix-inversion ADMM conquers the computational bottlenecks of the conventional imaging model. It approximates the observation matrix via the imaging operator  $\mathbf{I}(\cdot)$  and the observation operator  $\mathbf{G}(\cdot)$ . Building upon this, matrix inversion is replaced by a linear computation derived from Taylor expansion, enabling efficient 2D data processing. For model adaptability, we employ a generalized regularization function  $\phi(\cdot)$  and solve its subproblem through a nonlinear proximal operator  $\mathcal{F}_\Theta(\cdot)$ . This lays a foundation for the ARSAR-Net in the next Section.

### III. ADAPTIVELY REGULARIZED IMAGING NETWORK

Based on the non-matrix-inversion ADMM, we present the adaptive regularized SAR imaging network (ARSAR-Net) with variants: ARSAR-Net Swift for enhanced imaging efficiency, and ARSAR-Net Pro for superior imaging quality.

#### A. Network Architecture

In Sec. II-C, we developed a non-matrix-inversion ADMM for 2D SAR imaging. Nevertheless, this iterative framework contains multiple hyperparameters that require manual tuning. In addition, the feasibility of the regularization function is challenged in complex scenes. To address these challenges, we unfold the iterative framework into a deep unfolding network, referred to as ARSAR-Net, where each layer strictly corresponds to an iteration step. Different from the conventional model-driven methods, this network supports the data-driven parameter optimization upon SAR echo data and ground truth image pairs.

As illustrated in Fig. 4, ARSAR-Net uses 2D SAR echo data  $\mathbf{Y}_d$  as input and outputs the scattering coefficient matrix  $\mathbf{X}^{(N)}$  (where the magnitude matrix of scattering coefficients serves

as the SAR image). The network consists of  $N_s$  layers, each containing three differentiable modules which correspond to the three variables solved in the non-matrix-inversion ADMM. The differentiable modules are detailed as follows.

1) **Reconstruction Module**: : This module, designed upon Eq. 15a, reconstructs the scattering coefficient matrix  $\mathbf{X}$  by replacing the matrix inversion operation with a linear computation. Specifically, CSA operators derived from the SAR system parameters enforce physical constraints following the imaging principles. The computational process of the module is

$$\begin{aligned} \mathbf{X}^{(k)} = & (1 - \tilde{\rho})\mathbf{X}^{(k-1)} + \mathbf{I} [\mathbf{Y}_d - \mathbf{G}(\mathbf{X}^{(k-1)})] \\ & + \tilde{\rho}(\mathbf{Z}^{(k-1)} - \mathbf{V}^{(k-1)}), \end{aligned} \quad (16)$$

where  $\mathbf{X}^{(k-1)}$ ,  $\mathbf{Z}^{(k-1)}$ ,  $\mathbf{V}^{(k-1)}$  and  $\mathbf{Y}_d$  denote the input variables,  $\mathbf{X}^{(k)}$  corresponds to the reconstructed output, and

- $\mathbf{I}(\cdot)$ : Imaging operator derived from CSA;
- $\mathbf{G}(\cdot)$ : Observation operator derived from CSA;
- $\tilde{\rho}$ : Network-shared learnable penalty parameter.

2) **Adaptive Regularizer Module**: : This module, derived from Eq. 15b, iteratively updates  $\mathbf{Z}$ . It employs a neural network to construct the nonlinear projection operator  $\mathcal{F}_\Theta(\cdot)$  for regularization, as

$$\mathbf{Z}^{(k)} = \mathcal{F}_\Theta(\mathbf{X}^{(k)} + \mathbf{V}^{(k-1)}), \quad (17)$$

where  $\mathbf{X}^{(k)}$ ,  $\mathbf{V}^{(k-1)}$  denote the input variables and  $\mathbf{Z}^{(k)}$  the reconstructed output variable. The detailed implementation of  $\mathcal{F}_\Theta(\cdot)$  will be presented in Sec. III-B.

3) **Scaled Multiplier Module**: :

This module updates the scaled dual variable  $\mathbf{V}$  by introducing a learnable, network-shared update rate  $\tilde{\eta}$ , which serves as an enhanced implementation of the standard formulation in Eq. 15c. This modification ensures stable convergence across network layers. The computational process is formulated as

$$\mathbf{V}^{(k)} = \mathbf{V}^{(k-1)} + \tilde{\eta}(\mathbf{X}^{(k)} - \mathbf{Z}^{(k)}), \quad (18)$$

where  $\mathbf{X}^{(k)}$ ,  $\mathbf{Z}^{(k)}$ ,  $\mathbf{V}^{(k-1)}$  denote the input variables, and  $\mathbf{V}^{(k)}$  the updated scaled dual variable. ARSAR-Net avoids manual parameter tuning through automated optimization of three modules. Distinct from conventional deep networks, ARSAR-Net constructs its network architecture based on the ADMM unfolding framework, thus enjoying better interpretability.

#### B. Adaptive Regularizer

Given  $\mathbf{X}$ ,  $\mathbf{Z}$ , and  $\mathbf{V}$  denoting 2D complex matrices in the network, ARSAR-Net employs specialized components for efficient complex-valued 2D data processing. The nonlinear projection operator  $\mathcal{F}_\Theta$  in Eq. 17 is implemented through three components: convolutional layers for feature extraction, activation functions for inducing nonlinear mappings, and normalization layers for training stability.

As these components exclusively operate on real-valued data, we adopt a channel-expansion strategy by decomposing each complex matrix into separate real and imaginary

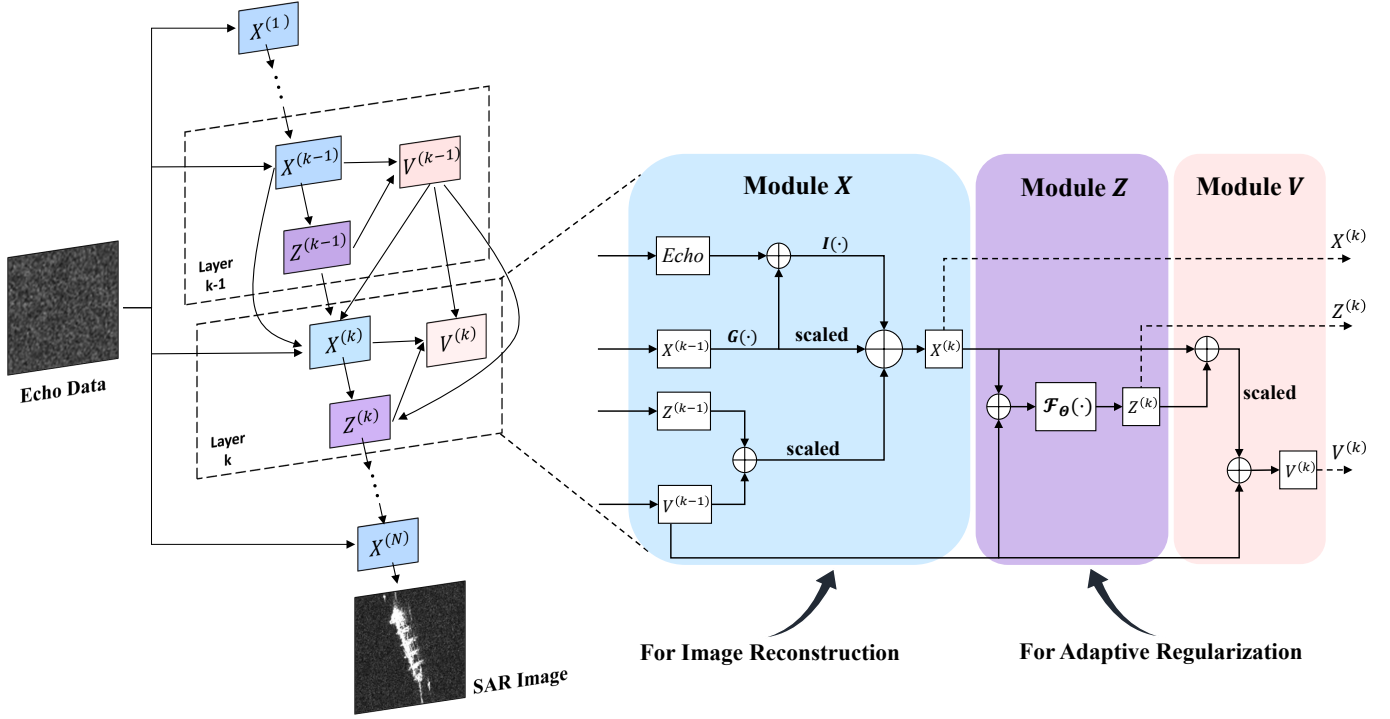


Fig. 4. Architecture of ARSAR-Net, which consists of a reconstruction module ( $\mathbf{X}$ ), an adaptive regularizer module ( $\mathbf{Z}$ ), and a scaled multiplier module ( $\mathbf{V}$ ).

channels. This changes the data dimensions from  $[B, H, W]$  to  $[B, C, H, W]$ , where  $B$  is the batch size,  $H/W$  denotes spatial dimensions, and  $C$  denotes the channel dimension. The subsequent operation recombines the two separated channels, restoring the original  $[B, H, W]$  dimensional structure.

We define two variants of ARSAR-Net: ARSAR-Net Swift for imaging efficiency and ARSAR-Net Pro for imaging quality. As shown in Fig. 5, these variants use different architectures in the adaptive regularizer modules while sharing two core modules.

1) **ARSAR-Net Swift**: This module integrates a pyramid structure with multi-scale fusion blocks to reduce computational costs. The characteristics of this variant include:

- **Pyramid Structure**: As shown Fig. 5, this structure achieves feature map downsampling through two specialized convolutional modules. The first module,  $\mathcal{C}_1$ , consists of a convolutional layer with a kernel size of 3, followed by batch normalization (BN) [52] and a ReLU activation function [53], specifically designed to reduce spatial resolution. The second module,  $\mathcal{C}_2$ , employs a convolutional layer with a kernel size of 1 to expand the channel dimensions while preserving spatial resolution. The dimensional transformations in feature maps induced by these modules are as follows:

$$\begin{aligned} [B, C, H, W] &\xrightarrow{\mathcal{C}_1} [B, C, H/2, W/2] \\ [B, C, H/2, W/2] &\xrightarrow{\mathcal{C}_2} [B, 2C, H/2, W/2] \end{aligned}$$

- **Multi-scale Feature Fusion**: The multi-scale fusion block first applies interpolation-based upsampling to the down-sampled feature maps, then concatenates them with the

same-scale feature maps along the channel dimension. The fused features are then passed through the convolutional module  $\mathcal{C}_3$ , which maintains spatial resolution while compressing channels. This process is expressed as

$$\begin{aligned} \sigma_{out}^{(i)} = \text{Fusion}(\sigma^{(i)}, \sigma_{out}^{(i+1)}) &= \mathcal{C}_3 \left[ \sigma^{(i)} \oplus \text{Up}(\sigma_{out}^{(i+1)}) \right] \\ [B, C, H/2, W/2] &\xrightarrow{\text{Up}} [B, C, H, W] \\ [B, 2C, H, W] &\xrightarrow{\mathcal{C}_3} [B, C, H, W] \end{aligned}$$

where  $\sigma^{(i)}$  represents the  $i$ -th feature maps in the pyramidal structure,  $\sigma_{out}^{(k)}$  denotes the  $i$ -th feature maps after upsampling,  $\text{Up}(\cdot)$  refers to bilinear interpolation-based upsampling, and  $\oplus$  denotes channel-wise concatenation.

2) **ARSAR-Net Pro**: This module employs a symmetric architecture that maintains consistent feature resolution across network layers, enhancing detail preservation at the cost of computational efficiency. The main characteristics of this variant include:

- **Full-resolution Connectivity**: This variant maintains full-resolution feature propagation across all network layers, effectively mitigating loss of image details. It also uses a convolutional cell  $\mathcal{C}_p$  composed of stacked convolutional layers with a kernel size of 3 and activation functions. This cell avoids feature map downsampling while progressively expanding channel dimensions. The dimensional transformation induced by the convolutional cell follows.

$$[B, C, H, W] \xrightarrow{\mathcal{C}_p} [B, 2C, H, W]$$

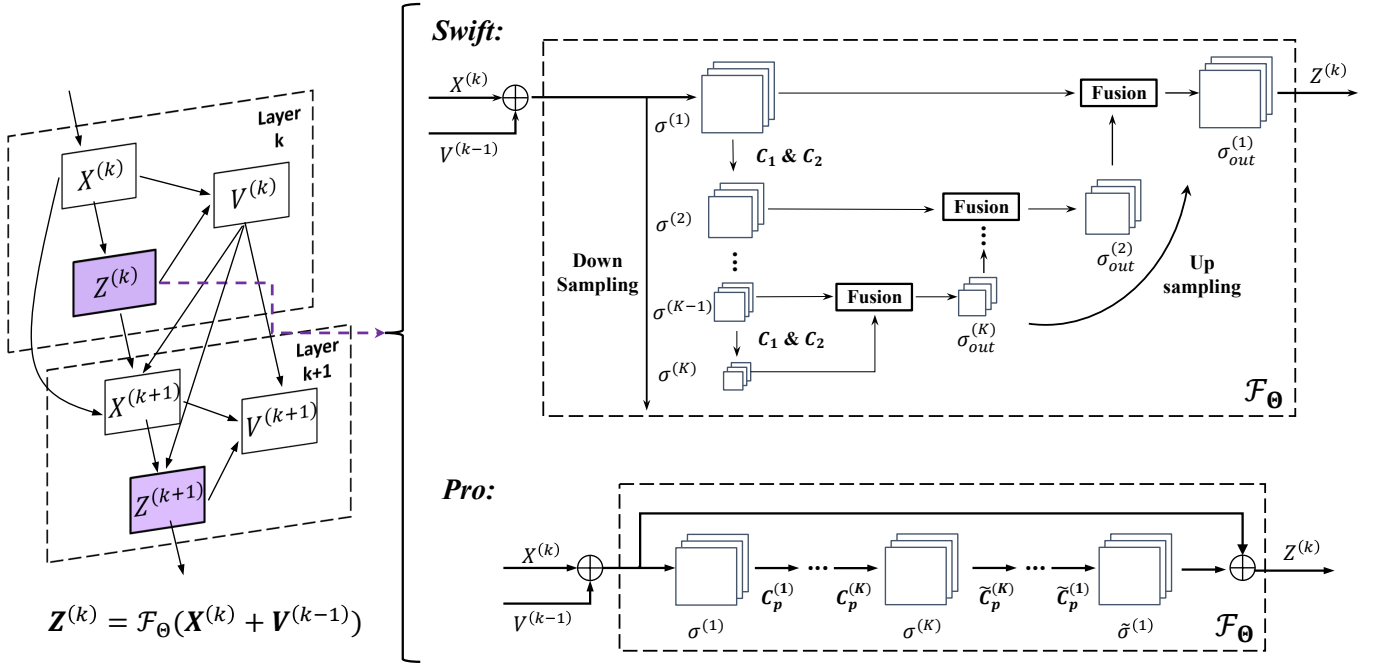


Fig. 5. Two variants of ARSAR-Net. ARSAR-Net Swift is specified for imaging efficiency, and ARSAR-Net Pro is specified for imaging quality.

- *Symmetric Structural Module:* To ensure that the Adaptive Regularization Module's input and output have consistent channel dimensions, we construct a symmetric module  $\tilde{C}_p$  which mirrors the convolution cell. This mirrored module employs convolutional layers to reduce channel dimensions progressively. The dimensional transformation induced by the convolution module is as

$$[B, 2C, H, W] \xrightarrow{\tilde{C}_p} [B, C, H, W]$$

- *Skip-connection Architecture:* This variant establishes an identity mapping, which allows gradients to flow directly through shortcut paths during training [54]. The Adaptive Regularization Module consists of  $K$  convolutional module pairs  $\{C_p^{(i)}, \tilde{C}_p^{(i)}\}_{i=1}^K$ , where each pair comprises a convolutional cell  $C_p^{(i)}$  and its symmetric module  $\tilde{C}_p^{(i)}$ . Collectively, these modules form the composite structure  $C_{total}$ . We introduce skip-connections that establish an identity mapping external to  $C_{total}$  structure, preserving details and accelerating network convergence. This design is formulated as

$$\begin{aligned} C_{total} &= C_p^{(1)} C_p^{(2)} \dots C_p^{(K)} \tilde{C}_p^{(K)} \dots \tilde{C}_p^{(2)} \tilde{C}_p^{(1)} \\ \sigma_{final} &= \sigma^{(1)} + \tilde{\sigma}^{(1)} = \sigma^{(1)} + C_{total}(\sigma^{(1)}) \end{aligned}$$

where  $\sigma^{(1)}$  denote input feature maps,  $\tilde{\sigma}^{(1)}$  feature maps after processing by  $C_{total}$  and  $\sigma_{final}$  output feature maps.

### C. Network Training

1) *Loss function:* The training dataset consists of  $N_{trn}$  samples, each defined as a pair  $(Y_i, X_i)$ , where  $Y_i$  represents a complex-valued SAR echo signal and  $X_i$  its corresponding ground truth image. Conventional loss functions, such as Mean

Squared Error (MSE), exhibit disadvantages for complex-valued SAR image reconstruction. To bridge this gap, we introduce the Normalized Mean Perceived Error (NMPE), a specialized loss function designed to be both compatible with complex signals and computationally efficient, as

$$\mathcal{L} = \frac{1}{N_{trn}} \sum_{i=1}^{N_{trn}} \frac{\frac{1}{H \times W} \sum_{p=1}^H \sum_{q=1}^W (|\hat{X}_i(p, q)| - |X_i(p, q)|)^2}{\|X_i\|_2} \quad (19)$$

where  $\hat{X}_i$  and  $Y_i$  respectively denote ARSAR-Net's output and the input echo.  $\|\cdot\|_2$  denotes the  $\ell_2$ -norm.

2) *Training Configuration:* We implement ARSAR-Net in the PyTorch framework [55], using the Adam optimizer [56] with a learning rate of  $2e-5$  across 80 training epochs. Both variants of ARSAR-Net share identical configurations: a 9-layer architecture and a batch size of 4 during training.

## IV. EXPERIMENT

In this section, we validate the superiority of ARSAR-Net upon both simulated and real data, through experiments on both simulated distributed targets (Sec. IV-B) and real data (Sec. IV-C). We also discuss the convergence rate of ARSAR-Net in Sec. IV-D.

### A. Experimental Setting

1) *SAR System Parameters:* All the real SAR data used in the experiment are acquired from GaoFen-3, China's first C-band polarimetric SAR satellite, which supports 12 imaging modes and quad-polarization. Key parameters of this system are given in table I, which are also adopted in the generation of the simulated echo data.

TABLE I  
MAIN PARAMETERS OF THE SAR SYSTEM

Parameter	Value
Signal bandwidth	60 MHz
Pulse width	45 $\mu$ s
Pulse repetition frequency	1420 Hz
Carrier frequency	5.4 GHz
Slant range	850 km
Equivalent velocity	7500 m/s

TABLE II  
DATASET CONFIGURATION

Label	Training	Testing
Off-shore Ships	800	200
Harbors	400	100
Cities	400	100

2) *Experimental Platform*: All the experiments are conducted on a platform with Intel Xeon Gold 5320 CPU (2.20 GHz) and NVIDIA A100-80GB GPU.

3) *Dataset*: For network training, we construct a dataset from SAR single-look complex (SLC) images at 1m resolution acquired by the Gaofen-3 satellite. This dataset consists of 2,000 images categorized into three distinct scenes: offshore ships, harbors, and cities. These data are divided into 1,600 training samples and 400 test samples, shown in Table II, with each image standardized to  $512 \times 512$  pixels through cropping.

The CSA inverse imaging operator, configured using SAR system parameters from Table I, generates simulated echo signals that serve as network inputs, while the corresponding SLC images are used as ground truth. The range-direction sampling rate is constrained by the transmitted signal bandwidth, whereas the azimuth-direction sampling regulated by the pulse repetition frequency (PRF) offers greater operational flexibility [57]. This inherent characteristic renders azimuth downsampling particularly advantageous for practical implementation, compressing acquired information without compromising image quality. We utilize a random matrix as the downsampling matrix  $\Psi$ , which has been proven to meet the RIP conditions [58] [59]. Through random sampling, we generate azimuth-downsampled echoes at 50% and 75% of full sampling rates, which are subsequently used for network training and testing.

4) *Evaluation Metrics*: To quantitatively evaluate the performance of ARSAR-Net, the following evaluation metrics are employed: NRMSE [60], Peak Signal-to-Noise Ratio (PSNR, measured in dB), and Structural Similarity Index for Measuring (SSIM) [61]<sup>3</sup>.

## B. Distributed Target Simulation

Two simulation experiments are carried out to evaluate ARSAR-Net and compare it with representative methods, including the CSA-based method [50],  $\ell_1$ -Norm [39], and total variation (TV) regularization [40], as well as unfolding

network-based methods (LRSR-ADMM-Net [36] and SR-CSA-Net [38]). Azimuth downsampling is an effective strategy for reducing data storage and transmission demands in the SAR system. In these experiments, the simulated echoes are azimuth-downsampled at two rates (50% and 75%) to assess imaging performance under varying sampling conditions, with quantitative results summarized in Table III. For a fair comparison, all methods use identical downsampled echo data under consistent experimental settings.

With 50% downsampling, shown in Fig. 6, all methods exhibit noticeable artifacts and ambiguity. Conventional methods, including CSA,  $\ell_1$ -Norm, and TV regularization, demonstrate suboptimal imaging performance, with lower PSNR and SSIM values, alongside higher NRMSE values, indicating significant deviations from the ground truth. These deviations are particularly apparent in the azimuth direction. LRSR-ADMM-Net shows poor performance, whereas SR-CSA-Net achieves moderate improvements. The visual results reveal partial suppression of azimuth ambiguities and enhanced edge definitions. The proposed ARSAR-Net Swift substantially improves imaging quality. It mitigates the azimuth ambiguity while recovering edge structures aligned with the ground truth. Notably, the ARSAR-Net Pro variant achieves state-of-the-art performance, with a PSNR of 24.54 dB, SSIM of 0.862, preserving fine details and maintaining structural similarity up to 86% relative to ground truth.

Under the 75% downsampling condition, imaging performance improves across all methods. Conventional approaches exhibit moderate quality, yet still suffer from detail loss and azimuth ambiguity. Unfolding network-based methods, such as SR-CSA-Net, yield stronger imaging performance with fewer distortions and improved edge fidelity, reaching a PSNR value above 22.78 dB and an SSIM value exceeding 0.861. ARSAR-Net Swift delivers superior results, effectively suppressing ambiguities while recovering detailed structures. Meanwhile, ARSAR-Net Pro achieves the highest imaging quality, with a PSNR of 32.41 dB, SSIM of 0.948, maintaining fine textures and overall structural consistency with the ground truth. Both variants demonstrate robust generalization and strong performance in preserving image fidelity.

## C. Imaging in Real Scenes

1) *Overall dataset*: The first experiment is carried out on the overall dataset under two sampling rates (50% and 75%), comparing its performance against a range of conventional and unfolding network-based methods. The conventional methods include the CSA-based imaging operators method, and regularization techniques such as  $\ell_1$ -norm and TV approaches. Among deep learning baselines, we include unfolding network-based methods like LRSR-ADMM-Net and SR-CSA-Net for a more comprehensive comparison. The overall dataset contains a diverse mix of real-world SAR scenes, covering both sparse and non-sparse scenes. Experimental results are included in Table IV.

In Fig. 7, reconstruction results suffer from the azimuth ambiguity under the 50% sampling rate. The CSA-based imaging operators (Fig. 7b) show limited capability in suppressing ambiguities. The TV regularization method (Fig. 7d)

<sup>3</sup>Please refer to Appendix B for definitions of these evaluation metrics.

TABLE III  
COMPARISON OF IMAGING PERFORMANCE UNDER SAMPLING RATES FOR SIMULATION SCENES

Method	50% Sampling Rate			75% Sampling Rate		
	NRMSE	PSNR	SSIM	NRMSE	PSNR	SSIM
CSA	0.605	12.52	0.424	0.460	14.99	0.485
$\ell_1$ -Norm	0.521	14.16	0.574	0.203	20.04	0.791
TV	0.544	13.37	0.512	0.374	16.53	0.608
LRSR-ADMM-Net	0.722	11.32	0.375	0.418	15.61	0.491
SR-CSA-Net	0.209	20.24	0.683	0.159	22.78	0.861
ARSAR-Net Swift	0.239	18.83	0.685	0.086	28.17	0.861
ARSAR-Net Pro	<b>0.140</b>	<b>24.54</b>	<b>0.862</b>	<b>0.047</b>	<b>32.41</b>	<b>0.948</b>

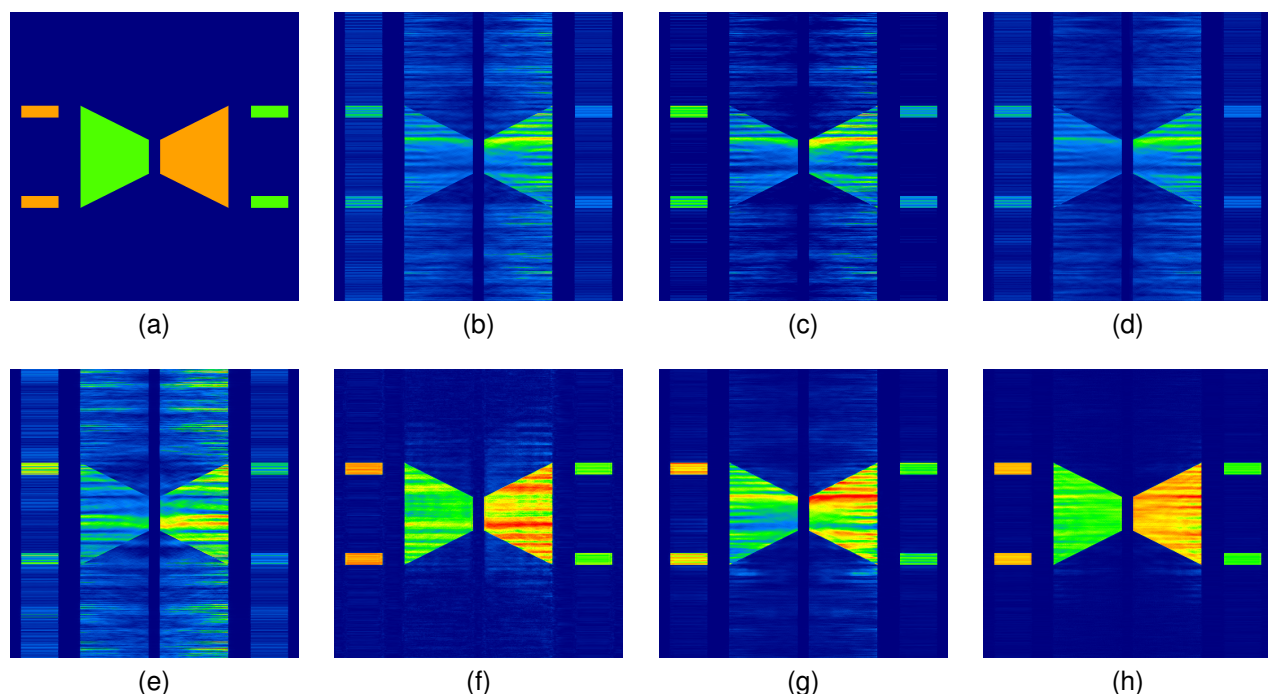


Fig. 6. Simulated scene results in different methods with 50% sampling rate. (a) ground truth. (b) CSA. (c)  $\ell_1$ -Norm. (d) TV. (e) LRSR-ADMM-Net. (f) SR-CSA-Net. (g) ARSAR-Net Swift. (h) ARSAR-Net Pro.

is effective at suppressing gradient variations induced by noise, but experiences difficulty in handling more severe ambiguities. In contrast, the  $\ell_1$ -norm method (Fig. 7c) demonstrates better suppression of the ambiguity in sparse scenes due to its sparsity-promoting nature. However, it tends to eliminate a substantial amount of fine detail, resulting in compromised structural fidelity in non-sparse scenes. Unfolding networks enhance imaging quality through a data-driven fashion. LRSR-ADMM-Net and SR-CSA-Net (Figs. 7e and 7f) show moderate improvements, achieving better suppression of azimuth ambiguities while preserving structural details. The proposed ARSAR-Net Swift (Fig. 7g) demonstrates high imaging quality across different scene types. However, the use of downsampling operations in the feature extraction stage inevitably leads to the loss of fine details. ARSAR-Net Pro (Fig. 7h) achieves

superior performance, with a PSNR of 30.75 dB, SSIM of 0.810, outperforming other methods with large margins.

The azimuth ambiguity is significantly reduced under the 75% sampling rate, leading to noticeable improvements in image quality, shown in Fig. 8. Conventional methods (Figs. 8b, 8c and 8d) show moderate enhancement compared to the 50% case, but shortcomings such as detail loss and residual ambiguities remain apparent. SR-CSA-Net, ARSAR-Net Swift, and ARSAR-Net Pro deliver high reconstruction quality under the 75% sampling rate. Notably, ARSAR-Net Pro (Fig. 8h) achieves state-of-the-art performance, attaining a PSNR of 36.05 dB and SSIM of 0.928, while maintaining fine textures and robust structural consistency.

The imaging speed is an important factor in practical systems. While the CSA-based imaging operators attain the

TABLE IV  
COMPARISON OF IMAGING PERFORMANCE UNDER SAMPLING RATES FOR REAL SCENES

Method	50% Sampling Rate			75% Sampling Rate			Imaging Speed (items/s)
	NRMSE	PSNR	SSIM	NRMSE	PSNR	SSIM	
CSA	0.384	24.02	0.539	0.287	26.78	0.693	210.2
$\ell_1$ -Norm	0.675	22.79	0.286	0.676	24.01	0.318	3.656
TV	0.377	24.07	0.550	0.276	26.36	0.694	3.371
LRSR-ADMM-Net	0.349	24.11	0.543	0.186	27.00	0.688	1.947
SR-CSA-Net	0.162	28.91	0.756	0.077	34.17	0.903	43.84
ARSAR-Net Swift	0.089	29.15	0.743	0.062	33.29	0.881	<b>67.60</b>
ARSAR-Net Pro	<b>0.084</b>	<b>30.75</b>	<b>0.810</b>	<b>0.036</b>	<b>36.05</b>	<b>0.928</b>	17.60

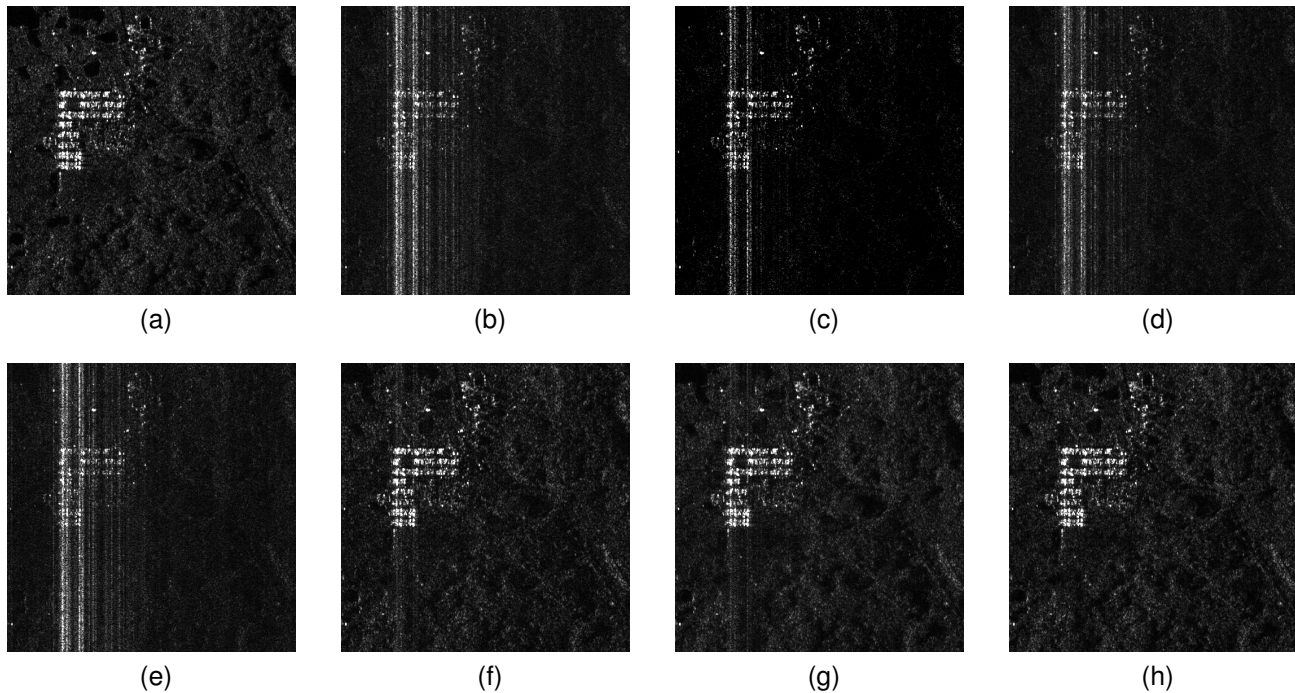


Fig. 7. Real sparse scene results in different methods with 50% sampling rate. (a) ground truth. (b) CSA. (c)  $\ell_1$ -Norm. (d) TV. (e) LRSR-ADMM-Net. (f) SR-CSA-Net. (g) ARSAR-Net Swift. (h) ARSAR-Net Pro.

highest imaging speed of 210.2 items/s, they suffer from low image quality. Conventional approaches suffer from low efficiency due to their iterative optimization procedures requiring repeated updates. The unfolding network, LRSR-ADMM-Net, is bottlenecked by the singular value decomposition operations, whereas SR-CSA-Net achieves faster reconstruction through its deep unfolding architecture. Our ARSAR-Net Swift further optimizes efficiency with a pyramid-structured network, achieving a superior imaging speed of 67.60 items/s. ARSAR-Net Pro prioritizes reconstruction fidelity through a full-resolution architecture, delivering the highest precision at the cost of efficiency.

2) *Subsets about sparse and non-sparse scenes:* This experiment assesses adaptability in scenes of different sparsity. The compared approaches consist of a conventional method based on  $\ell_1$ -norm and two unfolding networks: LRSR-ADMM-Net

and SR-CSA-Net. To ensure a fair comparison, all data-driven methods are trained on the overall dataset. A summary of experimental results is provided in Table V. For the case of the 50% sampling rate, Fig. 9 and Fig. 10 illustrate the visual imaging results in sparse and non-sparse scenes, respectively.

The conventional method based on  $\ell_1$ -norm regularization shows strong noise and ambiguity suppression capabilities, but it suffers from a significant loss of image details. In simple sparse scenes, this approach performs poorly compared to unfolding network-based methods, with a PSNR drop of about 5.5 dB and an SSIM reduction of around 0.5. The detail loss becomes even more severe in complex non-sparse scenes, leading to a more substantial reduction of 10 dB in PSNR and 0.55 in SSIM compared to the best-performing method. Such significant declines in reconstruction accuracy render the  $\ell_1$ -norm method inadequate for SAR imaging under

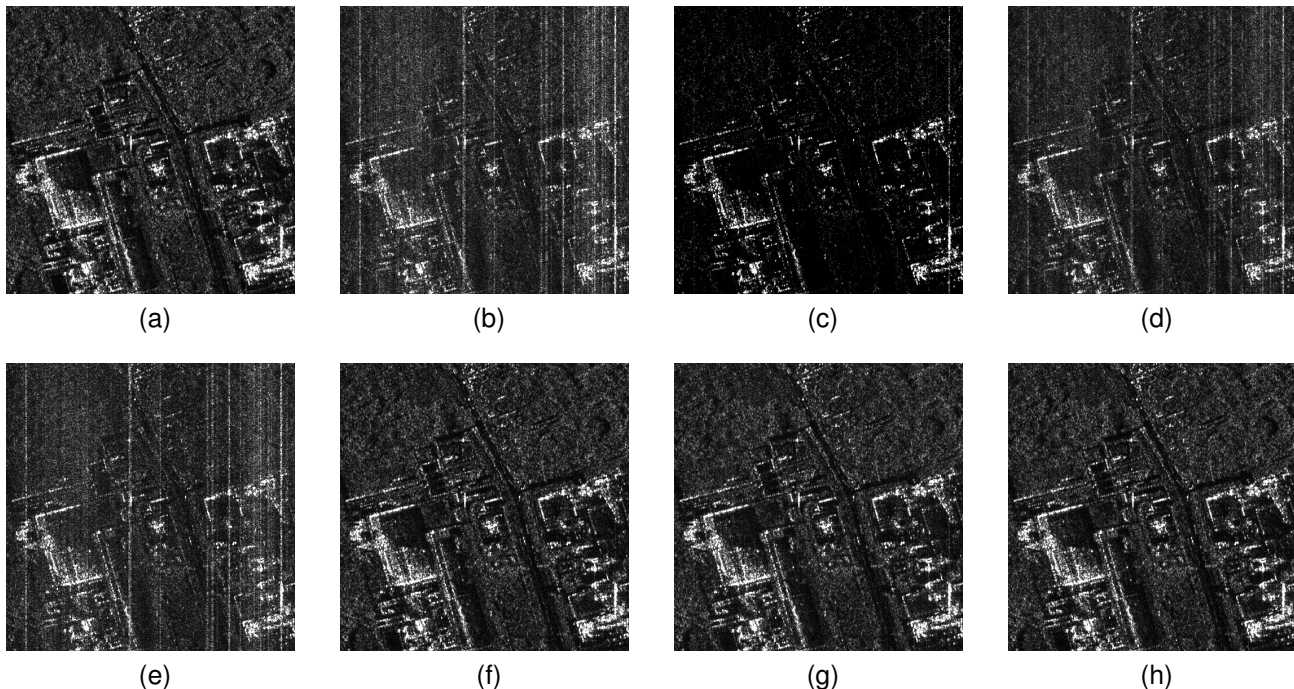


Fig. 8. Real non-sparse scene results in different methods with 75% sampling rate. (a) ground truth. (b) CSA. (c)  $\ell_1$ -Norm. (d) TV. (e) LRSR-ADMM-Net. (f) SR-CSA-Net. (g) ARSAR-Net Swift. (h) ARSAR-Net Pro.

TABLE V  
COMPARISON OF IMAGING PERFORMANCE UNDER SAMPLING RATES IN SUBSETS

Scene Type	Method	50% Sampling Rate			75% Sampling Rate		
		NRMSE	PSNR	SSIM	NRMSE	PSNR	SSIM
Sparse	$\ell_1$ -Norm	0.747	29.21	0.319	0.752	29.91	0.330
	LRSR-ADMM-Net	0.334	31.23	0.746	0.173	34.27	0.853
	SR-CSA-Net	0.278	32.91	0.777	0.147	35.98	0.877
	ARSAR-Net	<b>0.134</b>	<b>34.60</b>	<b>0.802</b>	<b>0.056</b>	<b>37.93</b>	<b>0.902</b>
Non-sparse	$\ell_1$ -Norm	0.615	18.24	0.277	0.611	19.93	0.328
	LRSR-ADMM-Net	0.355	19.07	0.397	0.191	21.89	0.567
	SR-CSA-Net	0.086	26.00	0.743	0.031	32.78	0.921
	ARSAR-Net	<b>0.050</b>	<b>28.01</b>	<b>0.817</b>	<b>0.023</b>	<b>34.65</b>	<b>0.947</b>

downsampled conditions.

LRSR-ADMM-Net achieves promising imaging quality in sparse scenes, with PSNR and SSIM values comparable to the best-performing method. Nevertheless, due to its limited parameter size and training capacity, its performance degrades in non-sparse scenes, e.g., PSNR dropping by about 9 dB and SSIM decreasing by 0.4 compared to ARSAR-Net. This substantial performance gap indicates that LRSR-ADMM-Net lacks adaptability to non-sparse scenes. By integrating an unfolding network with the CSA-based imaging operators, SR-CSA-Net achieves high imaging performance in both sparse and non-sparse scenes. The proposed ARSAR-Net further improves reconstruction fidelity through the adaptive regularizer module, outperforming existing methods by 2 dB PSNR. These results validate its generalization capacity across scenes.

3) *Network Layers setting*: ARSAR-Net is derived by unfolding the non-matrix-inversion ADMM, where each layer corresponds to an iteration. Therefore, the number of network layers  $N_s$  has a significant impact on both imaging speed (items/s) and reconstruction quality, which is summarized in Table VI.

In Fig. 12, the PSNR value of ARSAR-Net Swift increases gradually with network layers and begins to plateau around 29.2 dB when the depth exceeds 9. In contrast, ARSAR-Net Pro shows a sharp improvement in PSNR as the depth increases, eventually stabilizing at about 30.8 dB beyond 8 layers. On the other hand, the imaging speed of both variants decreases rapidly as the number of layers increases.

For the trade-off between quality and speed, we select a 9-layer network for both ARSAR-Net variants. This shows

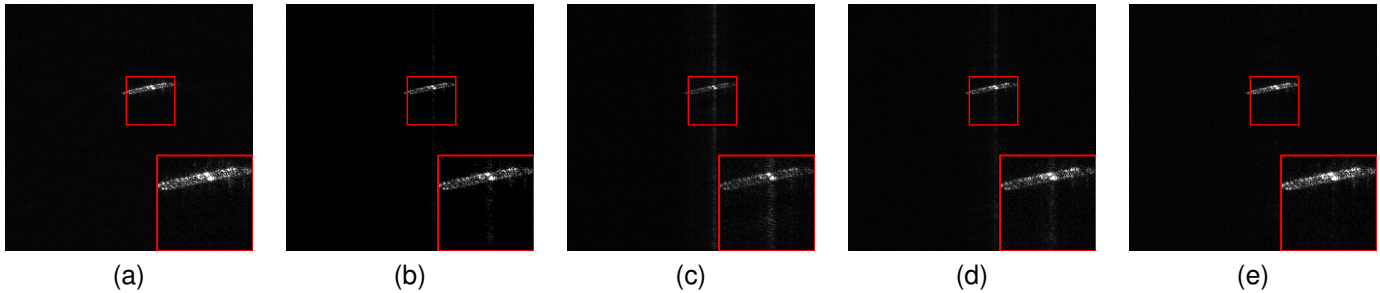


Fig. 9. Comparison of imaging results in a sparse scene. (a) ground truth. (b)  $\ell_1$ -Norm. (c) LRSR-ADMM-Net. (d) SR-CSA-Net. (e) ARSAR-Net.

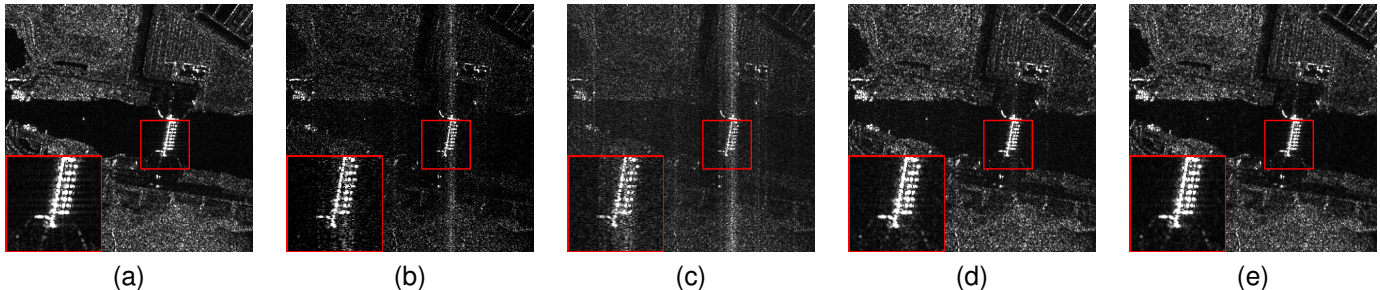


Fig. 10. Comparison of imaging results in a non-sparse scene. (a) ground truth. (b)  $\ell_1$ -Norm. (c) LRSR-ADMM-Net. (d) SR-CSA-Net. (e) ARSAR-Net.

TABLE VI  
PERFORMANCE OF ARSAR-NET VARIANTS UNDER DIFFERENT LAYER NUMBERS UNDER 50% DOWNSAMPLING RATE

Method	$N_s = 3$			$N_s = 6$			$N_s = 9$		
	PSNR	SSIM	Speed	PSNR	SSIM	Speed	PSNR	SSIM	Speed
ARSAR-Net Swift	28.64	0.728	154.0	28.99	0.739	71.23	29.15	0.743	67.60
ARSAR-Net Pro	24.03	0.540	33.28	29.20	0.783	21.92	30.75	0.810	17.60

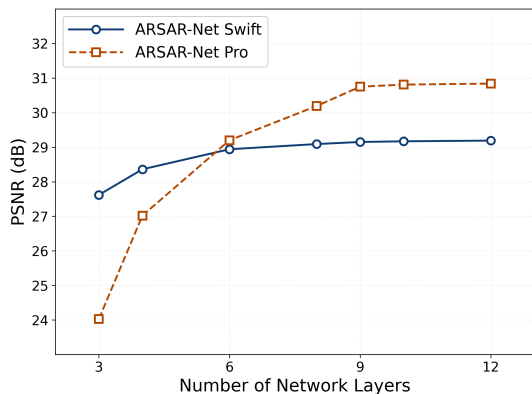


Fig. 11. PSNR under different layers

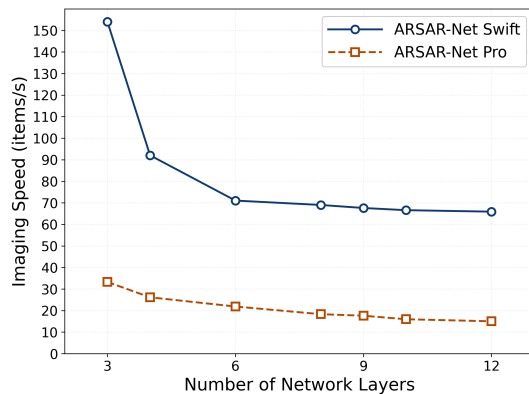


Fig. 12. Imaging speed under different layers

superior imaging performance compared to networks with fewer layers, while maintaining high imaging efficiency<sup>4</sup>.

As shown in Fig. 13, the outputs of ARSAR-Net Pro from layers 1, 3, 5, 7, and 9 demonstrate a progressive improvement in reconstruction quality under a 50% sampling rate.

<sup>4</sup>Please refer to Appendix C for the complexity analysis.

#### D. Training Convergence

During training, the compared unfolding networks demonstrate different convergence behaviors, illustrated in Fig. 14. LRSR-ADMM-Net exhibits a relatively flat and stable loss curve throughout training, indicating constrained adaptability due to the limited size of its trainable parameters. In contrast, SR-CSA-Net achieves rapid convergence in the early epochs,

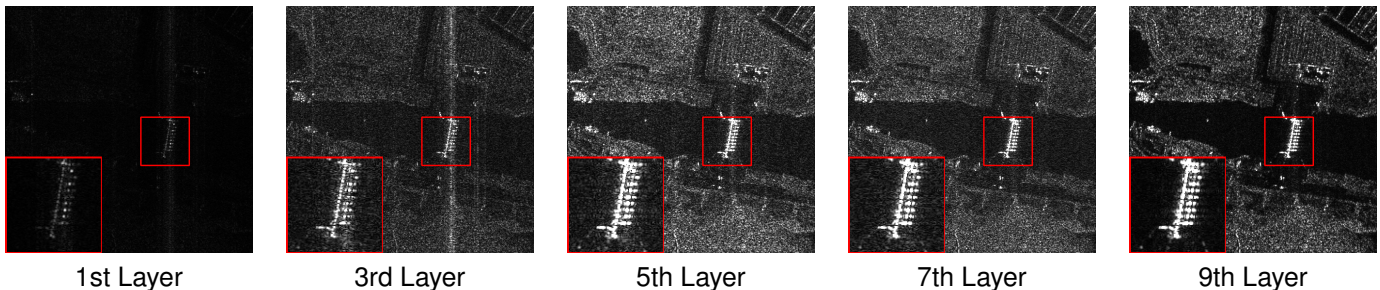


Fig. 13. Reconstruction results of ARSAR-Net Pro at different layers under 50% sampling rate.

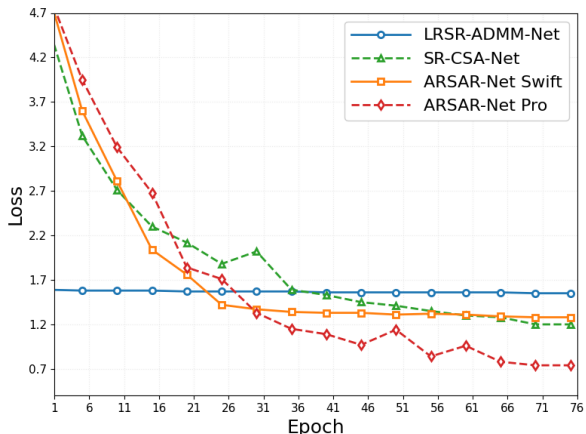


Fig. 14. Training loss curves of compared methods

with its loss decreasing from over 4.6 to 1.2 before stabilizing. This smooth convergence suggests strong learning capability, particularly during the early stages of training.

Meanwhile, ARSAR-Net Swift starts with the highest initial loss among all methods but shows a steady decline, indicating a stable training process with consistent improvements. While it does not achieve as low a final loss as ARSAR-Net Pro, its convergence trend remains reliable. ARSAR-Net Pro, by contrast, reaches the lowest loss (around 0.7), demonstrating strong optimization capability and superior training efficiency.

Overall, ARSAR-Net Pro enjoys the best convergence performance, achieving a balance between speed and final loss. In comparison, ARSAR-Net Swift converges more gradually, reflecting a stable and robust optimization process.

## V. CONCLUSION

We proposed an adaptively regularized SAR imaging network, ARSAR-Net, to address the limitations of regularization methods and baseline unfolding networks for adaptive SAR imaging. A non-matrix-inversion ADMM algorithm is adopted, in which matrix inversion is approximated by an efficient linear operation. Based on this algorithm, we propose an enhanced 2D SAR imaging model that integrates CSA operators. This model is then unfolded into a deep unfolding network, enabling the regularization module to be learned in an adaptive and efficient manner. Extensive experiments on simulated and real-world SAR data demonstrated the

superiority of our approach over conventional regularization-based methods and existing unfolding networks. Additionally, the computational complexity and convergence behavior of ARSAR-Net were systematically analyzed, highlighting its practical applicability. The proposed framework advances SAR imaging by integrating model-driven priors with data-driven adaptability, providing fresh insight for high-quality and efficient SAR imaging in complex scenes.

## APPENDIX A PROOF OF EQ. 13

We aim to simplify Eq. 12, which is expressed as follows.

$$\mathbf{X}^{(k)} = \arg \min_{\mathbf{X}} [\mathcal{S}(\mathbf{X}^{(k-1)}) + \nabla \mathcal{S}(\mathbf{X}^{(k-1)})^H (\mathbf{X} - \mathbf{X}^{(k-1)}) + \frac{L}{2} \|\mathbf{X} - \mathbf{X}^{(k-1)}\|_2^2]$$

We combine the linear and quadratic terms by completing the square, as shown in the following equation.

$$\begin{aligned} \mathbf{X}^{(k)} = \arg \min_{\mathbf{X}} & [\mathcal{S}(\mathbf{X}^{(k-1)}) + \nabla \mathcal{S}(\mathbf{X}^{(k-1)})^H (\mathbf{X} - \mathbf{X}^{(k-1)}) \\ & + \frac{L}{2} \|\mathbf{X} - \mathbf{X}^{(k-1)}\|_2^2 \\ & - \frac{1}{2L} \nabla \mathcal{S}(\mathbf{X}^{(k-1)})^H \nabla \mathcal{S}(\mathbf{X}^{(k-1)}) \\ & + \frac{1}{2L} \nabla \mathcal{S}(\mathbf{X}^{(k-1)})^H \nabla \mathcal{S}(\mathbf{X}^{(k-1)})] \end{aligned} \quad (20)$$

After simplification, we obtain the following result:

$$\begin{aligned} \mathbf{X}^{(k)} = \arg \min_{\mathbf{X}} & \left[ \frac{L}{2} \left\| \mathbf{X} - \mathbf{X}^{(k-1)} + \frac{1}{L} \nabla \mathcal{S}(\mathbf{X}^{(k-1)}) \right\|_2^2 \right. \\ & \left. + \mathcal{S}(\mathbf{X}^{(k-1)}) - \frac{1}{2L} \nabla \mathcal{S}(\mathbf{X}^{(k-1)})^H \nabla \mathcal{S}(\mathbf{X}^{(k-1)}) \right]. \end{aligned} \quad (21)$$

where  $\mathcal{S}(\mathbf{X}^{(k-1)})$ ,  $\frac{1}{2L} \nabla \mathcal{S}(\mathbf{X}^{(k-1)})^H \nabla \mathcal{S}(\mathbf{X}^{(k-1)})$  are constant terms irrelevant to the optimization variable  $\mathbf{X}$ .

The constant terms independent of  $\mathbf{X}$  are omitted, as it does not affect the minimization, as

$$\mathbf{X}^{(k)} = \arg \min_{\mathbf{X}} \left[ \frac{L}{2} \left\| \mathbf{X} - \mathbf{X}^{(k-1)} + \frac{1}{L} \nabla \mathcal{S}(\mathbf{X}^{(k-1)}) \right\|_2^2 \right]. \quad (22)$$

By solving the minimization problem, we obtain an iterative solution in the form of a gradient descent step, as

$$\mathbf{X}^{(k)} = \mathbf{X}^{(k-1)} - \frac{1}{L} \nabla \mathcal{S}(\mathbf{X}^{(k-1)}). \quad (23)$$

The gradient of the objective function  $\mathcal{S}(\mathbf{X}^{(k)})$  is computed as follows. Since  $\mathbf{G}(\cdot)$  consists entirely of linear operations [38], we have  $\mathbf{G}^H(\cdot) = \mathbf{I}(\cdot)$ , which simplifies the gradient expression.

$$\begin{aligned} \nabla \mathcal{S}(\mathbf{X}^{(k)}) &= \nabla \left\| \mathbf{G}(\mathbf{X}^{(k)}) - \mathbf{Y}_d \right\|_2^2 \\ &\quad + \frac{\rho}{2} \nabla \left\| \mathbf{X}^{(k)} - \mathbf{Z}^{(k-1)} + \mathbf{V}^{(k-1)} \right\|_2^2 \\ &= 2\mathbf{G}^H[\mathbf{G}(\mathbf{X}^{(k)}) - \mathbf{Y}_d] \\ &\quad + \rho(\mathbf{X}^{(k)} - \mathbf{Z}^{(k-1)} + \mathbf{V}^{(k-1)}) \\ &= 2\mathbf{I}[\mathbf{G}(\mathbf{X}^{(k)}) - \mathbf{Y}_d] \\ &\quad + \rho(\mathbf{X}^{(k)} - \mathbf{Z}^{(k-1)} + \mathbf{V}^{(k-1)}), \end{aligned} \quad (24)$$

where the imaging operator  $\mathbf{I}(\cdot)$  is given by Equation (10).

Substituting the gradient expression into the iterative solution, we have

$$\begin{aligned} \mathbf{X}^{(k)} &= \mathbf{X}^{(k-1)} - \frac{2}{L} \mathbf{I}[\mathbf{G}(\mathbf{X}^{(k)}) - \mathbf{Y}_d] \\ &\quad - \frac{\rho}{L} (\mathbf{X}^{(k)} - \mathbf{Z}^{(k-1)} + \mathbf{V}^{(k-1)}) \\ &= (1 - \frac{\rho}{L}) \mathbf{X}^{(k-1)} + \frac{2}{L} \mathbf{I}[\mathbf{Y}_d - \mathbf{G}(\mathbf{X}^{(k)})] \\ &\quad + \frac{\rho}{L} (\mathbf{Z}^{(k-1)} - \mathbf{V}^{(k-1)}). \end{aligned} \quad (25)$$

After setting  $L = 2$ , the iterative solution simplifies to the following expression, which combines the previous estimate, the imaging residual, and the auxiliary variables, as

$$\begin{aligned} \mathbf{X}^{(k)} &= (1 - \frac{\rho}{2}) \mathbf{X}^{(k-1)} + \mathbf{I}[\mathbf{Y}_d - \mathbf{G}(\mathbf{X}^{(k)})] \\ &\quad + \frac{\rho}{2} (\mathbf{Z}^{(k-1)} - \mathbf{V}^{(k-1)}). \end{aligned}$$

## APPENDIX B

### DEFINITION OF EVALUATION METRICS

Let  $\hat{X}$  denote the reconstructed SAR image and  $X$  the ground truth. The mathematical formulations of these evaluation metrics are:

$$\text{NRMSE} = \frac{\sum_{i=1}^H \sum_{j=1}^W \|X(i, j) - \hat{X}(i, j)\|_2}{\sum_{i=1}^H \sum_{j=1}^W \|X(i, j)\|_2} \quad (26)$$

$$\text{PSNR} = 10 \log_{10} \left( \frac{\max_{1 \leq i \leq H, 1 \leq j \leq W} X(i, j)}{\frac{1}{N} \sum_{i=1}^H \sum_{j=1}^W (X(i, j) - \hat{X}(i, j))^2} \right) \quad (27)$$

$$\text{SSIM} = \frac{(2\mu_X \mu_{\hat{X}} + C_1)(2\sigma_{X\hat{X}} + C_2)}{(\mu_X^2 + \mu_{\hat{X}}^2 + C_1)(\sigma_X^2 + \sigma_{\hat{X}}^2 + C_2)}, \quad (28)$$

where  $X$  is the ground truth SAR image of size  $H \times W$ ,  $\hat{X}$  is the reconstructed image of size  $H \times W$ ,  $N = H \times W$  is the total pixel count.  $\mu_X = \frac{1}{N} \sum_{i=1}^N X_i$  and  $\mu_{\hat{X}} = \frac{1}{N} \sum_{i=1}^N \hat{X}_i$  denote local pixel means;  $\sigma_X^2 = \frac{1}{N-1} \sum_{i=1}^N (X_i - \mu_X)^2$  and  $\sigma_{\hat{X}}^2 = \frac{1}{N-1} \sum_{i=1}^N (\hat{X}_i - \mu_{\hat{X}})^2$  denote standard deviations;  $\sigma_{X\hat{X}} = \frac{1}{N-1} \sum_{i=1}^N (X_i - \mu_X)(\hat{X}_i - \mu_{\hat{X}})$  is cross-covariance;  $C_1 = (K_1 L)^2$ ,  $C_2 = (K_2 L)^2$ , and  $L$  is the pixel value range and equals 255 for 8-bit grayscale images. In the experiment, we set  $K_1 = 0.01$  and  $K_2 = 0.03$ .

## APPENDIX C

### COMPLEXITY ANALYSIS

Each layer of ARSAR-Net consists of three modules: a reconstruction module, an adaptive regularizer module, and the scaled multiplier module. The scaled multiplier module, based on linear computations, has low computational complexity. Therefore, we focus on analyzing the complexity of the other two modules.

Let us assume that the scattering coefficient matrix  $X$  is of size  $N \times N$ . According to Eq. 16, this module involves linear operations, the imaging operator  $\mathbf{I}$ , and the observation operator  $\mathbf{G}$ , as defined in Eq. 10 and Eq. 9, respectively. These operators mainly consist of Fourier transforms and element-wise matrix multiplications (Hadamard products). The computational complexity of a two-dimensional Fourier transform is  $\mathcal{O}(N^2 \log N)$  [62], while the complexity of element-wise matrix multiplication is  $\mathcal{O}(N^2)$ . Combining both operations, the overall complexity of this Module is

$$\mathcal{O}(N^2 \log N) + \mathcal{O}(N^2) = \mathcal{O}(N^2 \log N).$$

In the conventional ADMM algorithm, the computational bottleneck is matrix inversion, which has a complexity of  $\mathcal{O}(N^3)$ . By adopting the non-matrix-inversion ADMM algorithm, the reconstruction module reduces the complexity from  $\mathcal{O}(N^3)$  to  $\mathcal{O}(N^2 \log N)$ .

As described in Sec. III-B, ARSAR-Net consists of two variants, Swift and Pro, which differ in the architecture of their adaptive regularizer modules.

For the adaptive regularizer module in the Swift variant, the main burden arises from convolutional layers. The complexity of the convolutional operation is  $\mathcal{O}(N^2 \times C_{in} \times C_{out} \times K^2)$ , where  $C_{in}$  denotes the number of input feature channels,  $C_{out}$  denotes the number of output feature channels and  $K$  the convolution kernel size. With the kernel size  $K$  being negligible relative to the feature map size  $N$ , the convolution operation has a simplified complexity denoted as  $\mathcal{O}(N^2 \times C_{in} \times C_{out})$ . Although the convolutional layers increase the number of feature channels, the size of feature maps is reduced at the same rate, keeping the overall complexity  $\mathcal{O}(N^2)$ . In contrast, this module in the Pro variant retains a full-resolution structure. While the size of feature maps remains fixed, the number of channels increases progressively. When the number of channels reaches its maximum, the input and output channels satisfy  $C_{in} \times C_{out} \sim N$ . Therefore, the complexity of this module is

$$\mathcal{O}(N^2 \times C_{in} \times C_{out}) = \mathcal{O}(N^3).$$

Since the modules in ARSAR-Net are executed sequentially, the overall complexity is determined by the module with the highest complexity. Consequently, the computational complexity of ARSAR-Net Swift is

$$\mathcal{O}(N^2 \log N) + \mathcal{O}(N^2) = \mathcal{O}(N^2 \log N),$$

while that of ARSAR-Net Pro is

$$\mathcal{O}(N^2 \log N) + \mathcal{O}(N^3) = \mathcal{O}(N^3).$$

## REFERENCES

- [1] I. G. Cumming and F. H. Wong, "Digital processing of synthetic aperture radar data," *Artech house*, vol. 1, no. 3, pp. 108–110, 2005.
- [2] A. Moreira, P. Prats-Iraola, M. Younis, G. Krieger, I. Hajnsek, and K. P. Papathanassiou, "A tutorial on synthetic aperture radar," *IEEE Geoscience and remote sensing magazine*, vol. 1, no. 1, pp. 6–43, 2013.
- [3] R. P. Perry, R. C. DiPietro, and R. L. Fante, "Sar imaging of moving targets," *IEEE Transactions on Aerospace and Electronic Systems*, vol. 35, no. 1, pp. 188–200, 2002.
- [4] M. Çetin, I. Stojanović, N. Ö. Önhon, *et al.*, "Sparsity-driven synthetic aperture radar imaging: Reconstruction, autofocusing, moving targets, and compressed sensing," *IEEE Signal Processing Magazine*, vol. 31, no. 4, pp. 27–40, 2014.
- [5] I. G. Cumming and S. Li, "Improved slope estimation for sar doppler ambiguity resolution," *IEEE transactions on geoscience and remote sensing*, vol. 44, no. 3, pp. 707–718, 2006.
- [6] R. Bamler, "A comparison of range-doppler and wavenumber domain sar focusing algorithms," *IEEE Transactions on Geoscience and Remote Sensing*, vol. 30, no. 4, pp. 706–713, 1992.
- [7] R. K. Raney, H. Runge, R. Bamler, I. G. Cumming, and F. H. Wong, "Precision sar processing using chirp scaling," *IEEE Transactions on geoscience and remote sensing*, vol. 32, no. 4, pp. 786–799, 1994.
- [8] Z. Jin, Z. Pan, Z. Zhang, and X. Qiu, "Saas-net: Self-supervised sparse synthetic aperture radar imaging network with azimuth ambiguity suppression.," *Remote Sensing*, vol. 17, no. 6, 2025.
- [9] V. Monga, Y. Li, and Y. C. Eldar, "Algorithm unrolling: Interpretable, efficient deep learning for signal and image processing," *IEEE Signal Processing Magazine*, vol. 38, no. 2, pp. 18–44, 2021.
- [10] I. Daubechies, M. DeFrise, and C. De Mol, "An iterative thresholding algorithm for linear inverse problems with a sparsity constraint," *Communications on Pure and Applied Mathematics: A Journal Issued by the Courant Institute of Mathematical Sciences*, vol. 57, no. 11, pp. 1413–1457, 2004.
- [11] S. Boyd, N. Parikh, E. Chu, B. Peleato, J. Eckstein, *et al.*, "Distributed optimization and statistical learning via the alternating direction method of multipliers," *Foundations and Trends® in Machine learning*, vol. 3, no. 1, pp. 1–122, 2011.
- [12] J. Fang, Z. Xu, B. Zhang, W. Hong, and Y. Wu, "Fast compressed sensing sar imaging based on approximated observation," *IEEE Journal of Selected Topics in Applied Earth Observations and Remote Sensing*, vol. 7, no. 1, pp. 352–363, 2013.
- [13] R. Baraniuk and P. Steeghs, "Compressive radar imaging," in *2007 IEEE radar conference*, IEEE, 2007, pp. 128–133.
- [14] B. Zhang, W. Hong, and Y. Wu, "Sparse microwave imaging: Principles and applications," *Science China Information Sciences*, vol. 55, no. 8, pp. 1722–1754, 2012.
- [15] A. Ribes and F. Schmitt, "Linear inverse problems in imaging," *IEEE Signal Processing Magazine*, vol. 25, no. 4, pp. 84–99, 2008.
- [16] J. A. Tropp and A. C. Gilbert, "Signal recovery from random measurements via orthogonal matching pursuit," *IEEE Transactions on information theory*, vol. 53, no. 12, pp. 4655–4666, 2007.
- [17] D. Needell and J. A. Tropp, "Cosamp: Iterative signal recovery from incomplete and inaccurate samples," *Applied and computational harmonic analysis*, vol. 26, no. 3, pp. 301–321, 2009.
- [18] A. Beck and M. Teboulle, "A fast iterative shrinkage-thresholding algorithm for linear inverse problems," *SIAM journal on imaging sciences*, vol. 2, no. 1, pp. 183–202, 2009.
- [19] F. Shen, G. Zhao, Z. Liu, G. Shi, and J. Lin, "Sar imaging with structural sparse representation," *IEEE Journal of Selected Topics in Applied Earth Observations and Remote Sensing*, vol. 8, no. 8, pp. 3902–3910, 2014.
- [20] A. Soni and J. Haupt, "Learning sparse representations for adaptive compressive sensing," in *2012 IEEE International Conference on Acoustics, Speech and Signal Processing (ICASSP)*, IEEE, 2012, pp. 2097–2100.
- [21] S. Samadi, M. Çetin, and M. A. Masnadi-Shirazi, "Multiple feature-enhanced sar imaging using sparsity in combined dictionaries," *IEEE Geoscience and Remote Sensing Letters*, vol. 10, no. 4, pp. 821–825, 2012.
- [22] C. Jiang, B. Zhang, J. Fang, *et al.*, "Efficient  $l_q$  regularisation algorithm with range–azimuth decoupled for sar imaging," *Electronics Letters*, vol. 50, no. 3, pp. 204–205, 2014.
- [23] P. Wang, H. Zhang, and V. M. Patel, "Sar image despeckling using a convolutional neural network," *IEEE Signal Processing Letters*, vol. 24, no. 12, pp. 1763–1767, 2017.
- [24] Y. Li, C. Peng, Y. Chen, L. Jiao, L. Zhou, and R. Shang, "A deep learning method for change detection in synthetic aperture radar images," *IEEE Transactions on Geoscience and Remote Sensing*, vol. 57, no. 8, pp. 5751–5763, 2019.
- [25] Z. Zhang, H. Wang, F. Xu, and Y.-Q. Jin, "Complex-valued convolutional neural network and its application in polarimetric sar image classification," *IEEE Transactions on Geoscience and Remote Sensing*, vol. 55, no. 12, pp. 7177–7188, 2017.
- [26] J. Gao, B. Deng, Y. Qin, H. Wang, and X. Li, "Enhanced radar imaging using a complex-valued convolutional neural network," *IEEE Geoscience and Remote Sensing Letters*, vol. 16, no. 1, pp. 35–39, 2018.
- [27] Z.-j. Lu, Q. Qin, H.-y. Shi, and H. Huang, "Sar moving target imaging based on convolutional neural network," *Digital Signal Processing*, vol. 106, p. 102832, 2020.
- [28] H. Mu, Y. Zhang, C. Ding, Y. Jiang, M. H. Er, and A. C. Kot, "Deepimaging: A ground moving target imaging

- based on cnn for sar-gmti system,” *IEEE Geoscience and Remote Sensing Letters*, vol. 18, no. 1, pp. 117–121, 2020.
- [29] M. Wang, S. Wei, Z. Zhou, J. Shi, and X. Zhang, “Efficient admm framework based on functional measurement model for mmw 3-d sar imaging,” *IEEE Transactions on Geoscience and Remote Sensing*, vol. 60, pp. 1–17, 2022.
- [30] S. Wei, J. Liang, M. Wang, J. Shi, X. Zhang, and J. Ran, “Af-ampnet: A deep learning approach for sparse aperture isar imaging and autofocusing,” *IEEE Transactions on Geoscience and Remote Sensing*, vol. 60, pp. 1–14, 2021.
- [31] M. Wang, S. Wei, J. Liang, S. Liu, J. Shi, and X. Zhang, “Lightweight fista-inspired sparse reconstruction network for mmw 3-d holography,” *IEEE Transactions on Geoscience and Remote Sensing*, vol. 60, pp. 1–20, 2021.
- [32] H. Yang, Z. Huang, and Z. Zhang, “Interpretable attributed scattering center extracted via deep unfolding,” in *IGARSS 2024-2024 IEEE International Geoscience and Remote Sensing Symposium*, IEEE, 2024, pp. 2004–2008.
- [33] Y. Wu, R. Song, Z. Zhang, X. Qiu, and W. Yu, “Gsatnet: An azimuth ambiguity suppression network based on group sparsity and adaptive threshold for under-sampling sar imaging,” *IEEE Geoscience and Remote Sensing Letters*, 2024.
- [34] E. Mason, B. Yonel, and B. Yazici, “Deep learning for sar image formation,” in *Algorithms for Synthetic Aperture Radar Imagery XXIV*, SPIE, vol. 10201, 2017, pp. 11–21.
- [35] M. Li, J. Wu, W. Huo, *et al.*, “Target-oriented sar imaging for scr improvement via deep mf-admm-net,” *IEEE Transactions on Geoscience and Remote Sensing*, vol. 60, pp. 1–14, 2022.
- [36] H. An, R. Jiang, J. Wu, *et al.*, “Lrsr-admm-net: A joint low-rank and sparse recovery network for sar imaging,” *IEEE Transactions on Geoscience and Remote Sensing*, vol. 60, pp. 1–14, 2022.
- [37] L. Kang, T. Sun, Y. Luo, J. Ni, and Q. Zhang, “Sar imaging based on deep unfolded network with approximated observation,” *IEEE Transactions on Geoscience and Remote Sensing*, vol. 60, pp. 1–14, 2022.
- [38] H. Zhang, J. Ni, K. Li, Y. Luo, and Q. Zhang, “Non-sparse sar scene imaging network based on sparse representation and approximate observations,” *Remote Sensing*, vol. 15, no. 17, p. 4126, 2023.
- [39] N. Tsagkarakis, P. P. Markopoulos, G. Sklivanitis, and D. A. Pados, “L1-norm principal-component analysis of complex data,” *IEEE Transactions on Signal Processing*, vol. 66, no. 12, pp. 3256–3267, 2018.
- [40] F. I. Karahanoglu, I. Bayram, and D. Van De Ville, “A signal processing approach to generalized 1-d total variation,” *IEEE Transactions on Signal Processing*, vol. 59, no. 11, pp. 5265–5274, 2011.
- [41] S. V. Venkatakrishnan, C. A. Bouman, and B. Wohlberg, “Plug-and-play priors for model based reconstruction,” in *2013 IEEE global conference on signal and information processing*, IEEE, 2013, pp. 945–948.
- [42] A. M. Teodoro, J. M. Bioucas-Dias, and M. A. Figueiredo, “Image restoration and reconstruction using variable splitting and class-adapted image priors,” in *2016 IEEE International Conference on Image Processing (ICIP)*, IEEE, 2016, pp. 3518–3522.
- [43] Y. Fan, B. Zhang, and Y. Wu, “Integrating regularization and pnp priors for sar image reconstruction using multi-agent consensus equilibrium,” *IEEE Transactions on Geoscience and Remote Sensing*, 2024.
- [44] Y. Wang, Z. He, X. Zhan, Q. Zeng, and Y. Hu, “A 3-d sparse sar imaging method based on plug-and-play,” *IEEE Transactions on Geoscience and Remote Sensing*, vol. 60, pp. 1–14, 2022.
- [45] Y. Wu, Z. Zhang, X. Qiu, Y. Zhao, and W. Yu, “Mf-jmodl-net: A sparse sar imaging network for under-sampling pattern design towards suppressed azimuth ambiguity,” *IEEE Transactions on Geoscience and Remote Sensing*, 2024.
- [46] Y. Yang, J. Sun, H. Li, and Z. Xu, “Admm-csnet: A deep learning approach for image compressive sensing,” *IEEE transactions on pattern analysis and machine intelligence*, vol. 42, no. 3, pp. 521–538, 2018.
- [47] C. Space, *Sar 101: An introduction to synthetic aperture radar*, <https://www.capellaspace.com/blog/sar-101-an-introduction-to-synthetic-aperture-radar>, 2020.
- [48] E. J. Candes, J. K. Romberg, and T. Tao, “Stable signal recovery from incomplete and inaccurate measurements,” *Communications on Pure and Applied Mathematics: A Journal Issued by the Courant Institute of Mathematical Sciences*, vol. 59, no. 8, pp. 1207–1223, 2006.
- [49] R. Tomioka and M. Sugiyama, “Dual-augmented lagrangian method for efficient sparse reconstruction,” *IEEE Signal Processing Letters*, vol. 16, no. 12, pp. 1067–1070, 2009.
- [50] X. Dong and Y. Zhang, “A novel compressive sensing algorithm for sar imaging,” *IEEE Journal of selected topics in applied earth observations and remote sensing*, vol. 7, no. 2, pp. 708–720, 2013.
- [51] A. van den Bos, “Complex gradient and hessian,” *IEE Proceedings-Vision, Image and Signal Processing*, vol. 141, no. 6, pp. 380–382, 1994.
- [52] S. Ioffe and C. Szegedy, “Batch normalization: Accelerating deep network training by reducing internal covariate shift,” in *International conference on machine learning*, pmlr, 2015, pp. 448–456.
- [53] A. F. Agarap, “Deep learning using rectified linear units (relu),” *arXiv preprint arXiv:1803.08375*, 2018.
- [54] K. He, X. Zhang, S. Ren, and J. Sun, “Deep residual learning for image recognition,” in *Proceedings of the IEEE conference on computer vision and pattern recognition*, 2016, pp. 770–778.
- [55] N. Ketkar, J. Moolayil, N. Ketkar, and J. Moolayil, “Introduction to pytorch,” *Deep learning with python: learn best practices of deep learning models with PyTorch*, pp. 27–91, 2021.

- [56] D. P. Kingma and J. Ba, “Adam: A method for stochastic optimization,” *arXiv preprint arXiv:1412.6980*, 2014.
- [57] A. Moreira, “Suppressing the azimuth ambiguities in synthetic aperture radar images,” *IEEE Transactions on Geoscience and Remote Sensing*, vol. 31, no. 4, pp. 885–895, 1993.
- [58] R. Baraniuk, M. Davenport, R. DeVore, and M. Wakin, “A simple proof of the restricted isometry property for random matrices,” *Constructive approximation*, vol. 28, pp. 253–263, 2008.
- [59] J. Castorena and C. D. Creusere, “The restricted isometry property for banded random matrices,” *IEEE Transactions on Signal Processing*, vol. 62, no. 19, pp. 5073–5084, 2014.
- [60] A. A. Poli and M. C. Cirillo, “On the use of the normalized mean square error in evaluating dispersion model performance,” *Atmospheric Environment. Part A. General Topics*, vol. 27, no. 15, pp. 2427–2434, 1993.
- [61] A. Hore and D. Ziou, “Image quality metrics: Psnr vs. ssim,” in *2010 20th international conference on pattern recognition*, IEEE, 2010, pp. 2366–2369.
- [62] P. Duhamel and M. Vetterli, “Fast fourier transforms: A tutorial review and a state of the art,” *Signal processing*, vol. 19, no. 4, pp. 259–299, 1990.